Effect of Aluminum Flakes on Corrosion Protection Behavior of Water-Based Hybrid Zinc-Rich Coatings for Carbon Steel Substrate in NaCl Environment

Arthur Boidot [1,2], Frederic Gheno [2], Fouad Bentiss [1,3], Charafeddine Jama [1,*] and Jean-Bernard Vogt [1]

1   UMR 8207—UMET—Unité Matériaux et Transformations, Centrale Lille, INRAE, CNRS, University Lille, 59000 Lille, France
2   Nof Metal Coatings Europe SA, 120 Rue Galilée—CS 50093, CEDEX, 60106 Creil, France
3   Laboratory of Catalysis and Corrosion of Materials, Faculty of Sciences, Chouaib Doukkali University, P.O. Box 20, El Jadida M-24000, Morocco
*   Correspondence: charafeddine.jama@centralelille.fr

Abstract: In this study, waterborne hybrid organic-inorganic zinc rich coatings (ZRC) with different aluminum flake amounts were tested at low thickness in 3 wt% NaCl aqueous solution. Open circuit potential and impedance response evolution over time were measured experimentally to evaluate their anticorrosion properties. Microstructure of the investigated coatings and composition of the corrosion products were also determined by electron microscopy, X-ray diffraction and infrared spectroscopy, while the stability of the coatings was investigated via inductively coupled plasma optical emission spectroscopy. The results showed that the absence of aluminum flakes leads to a less stable matrix, unable to retain sufficient corrosion inhibitors, resulting in a shorter protection time. For an intermediate concentration of aluminum particles, good corrosion properties were observed. Corrosion products play an important role in the protection mechanism, with simonkolleite and hydrozincite accumulating over time, forming a protective layer on the substrate for several weeks. High amounts of aluminum also lead to the formation of corrosion products, but without providing a barrier effect, while rapidly consuming zinc, leading to rapid formula failure. These results indicate that the use of a controlled amount of aluminum flakes can significantly improve the corrosion protection capability of this type of coating.

Keywords: zinc rich coatings (ZRC); carbon steel; NaCl medium; electrochemical impedance spectroscopy; corrosion protection

1. Introduction

Zinc is a widely used metal in construction and transport fields for its anticorrosive properties. It might be used as a bulk material in some applications, as a zinc alloy, but it is mainly used in the form of coating through galvanizing. This presents two advantages, reducing the total amount of zinc used in the system and taking advantage of the low potential of zinc to provide a cathodic protection to the underlying substrate, in the case of steel. However, as the zinc reserves around the world are running low while extraction is increasing [1], mainly low-grade ores remain for zinc production according to recent simulations [2], which will lead to higher prices and supply problems. It is therefore increasingly important, both from an ecological and economic point of view, to reduce the amount used in anticorrosion coatings, while maintaining good protective properties.

Zinc-rich coatings (ZRC) are one way to achieve this, as they are high-performance anticorrosion films containing not only zinc, but also other components. They consist in embedding zinc particles into a binder, usually based, for example, on an organic resin, polyester or epoxy polymers [3–6], or an inorganic silicate-based product to form a polysiloxane network [3,7,8]. The final product is a composite coating, with metallic zinc pigments maintained together in a matrix.

The sol-gel coating process seems to be very well adapted to produce this matrix. A wide range of precursors is available for use as binders, which are adequately water-soluble and which ensure a very good dispersion of zinc particles [9–13]. In addition, this forms a mechanically resistant and thermally stable network with very good adhesion to several metal surfaces [14–16]. In some cases, hybrid binders combining both organic and inorganic functions are used, as they combine the properties of organic polymers, such as flexibility, and the advantages of inorganic coatings, including adhesion and thermal resistance [17–21].

The corrosion protection mechanisms of these coatings mostly depend on two phenomena [5,7,22]. Firstly, the cathodic effect will protect the steel substrate at earlier exposure stages. As long as there is an electrical contact between the zinc particles and the substrate, and the ratio between the active area of zinc and steel is sufficiently high, the mixed potential of the system will remain low enough to provide a cathodic protection [23,24]. The second effect slowly replaces the first, while the zinc particles are corroding. When the zinc oxidation occurs, it releases Zn ions that react with the surrounding electrolyte and form some corrosion products. These products are not electrical conductors and insulate the particles, reducing progressively the cathodic protection, but they also form a protective layer in the film. These corrosion products fill the defects in the coating and prevent the penetration of aggressive species through the coating to the substrate and provide a barrier effect to the coating after some time of exposure [25,26].

A high-volume concentration of pigment is required to ensure that an electrical contact is reached, both between the particles and with the substrate. Most commonly, zinc spherical particles are used, in a ratio of 70 to 90% by weight of these coatings [22,25,27]. Nowadays, other shapes of zinc particles are being used, such as zinc flakes, because their lamellar shape increases their specific surface area, while increasing the aggressive species penetration path through the layer [25]. This makes electrical contact between particles easier and means the percolation path is reached at lower zinc concentrations [25]. Other ways to improve the anticorrosive performance of the coatings while decreasing the zinc amount have been studied, such as replacing part of the zinc by fillers, such as clay or mica, in order to improve the barrier protection offered [28,29]. Another method to reduce the zinc amount while maintaining an electrical contact between the particles is the addition of conductive components, for example, carbon nanotubes or conductive polymers such as polyaniline [30,31] or even nanoparticles [32]. In this way, cathodic protection can be maintained even if the zinc particles do not touch each other, as long as an electrical percolation path to the substrate is created. Another approach is used in this paper, based on the use of aluminum flakes to replace part of the zinc. Several studies report good corrosion properties when adding a small amount of aluminum pigments [33,34]. Aluminum lamellae present several advantages, because aluminum has a very low potential when in metallic form and is very stable when an Al_2O_3 layer is formed on the surface. This stability in aqueous medium is a great advantage in water-based coatings during batch production and can be achieved with zinc, by making flakes of Zn-Al alloys, which provide good performance [35]. Aluminum lamellae are also aesthetically interesting, as they allow the formulation of a silver-gray color with a metallic effect due to the light reflecting on the surface of the flakes [36], which is of interest in the automobile industry.

While there are mainly durability issues with zinc, the same is true for the ZRC matrix. Indeed, most of the binders are based on volatile organic solvents, from ethanol to xylene [4,27,37]. These chemicals are both dangerous to human health and the environment, and legislation is evolving to reduce the amount of volatile organic compounds (VOCs) used in the industry [4,38]. Several trends observed limit those VOCs, such as the use of powder coatings to reduce the amount of solvents [39,40], and the development of water-based coatings [4,41].

In this work, industrial waterborne zinc-rich coatings with low thickness, and their corrosion mechanisms, were investigated. These coatings possess several features aforementioned: the binder is an innovative hybrid organic–inorganic sol-gel water-based

product, while the zinc particles are in a lamellar shape. This kind of binder is rarely found in the scientific literature and never in combination with metallic pigments of lamellar morphology, even though both sol-gel and flakes independently exhibit good anticorrosion properties. Moreover, the use of aluminum flakes in combination with zinc is uncommon and only reported for epoxy binders. Three formulations, containing different quantities of aluminum flakes, were studied using commentary characterization techniques. Electrochemical techniques such as open circuit potential (OCP) and electrochemical impedance spectroscopy (EIS) were performed in an aqueous solution of NaCl at 3 wt% to assess the properties of the coatings and their behavior during corrosion for 3 weeks. Inductively coupled plasma optical emission spectroscopy (ICP-OES) was used to determine the chemical species dissolving over time. Finally, structural characterization techniques such as X-ray diffraction (XRD), attenuated total reflectance Fourier-transform infrared spectroscopy (ATR-FTIR), and scanning electron microscopy (SEM) were used to study the corrosion products formed and the microstructure of the coatings.

2. Materials and Methods

2.1. Materials

2.1.1. Substrate

The coatings were applied on a DC01 (1.0330) EN10130 (NOF Metal Coatings, Creil, France) low-carbon cold rolled steel whose specified composition is given in Table 1. This steel grade was chosen for its low intrinsic corrosion resistance in NaCl medium as well as good availability and low price, making it a good candidate to receive an anticorrosion coating. The metal plates were first degreased in alkaline solution at 80 °C for 20 min, then scrubbed with GP-RL Scotch-Brite ™ sheets from 3M (Cergy-Pontoise, France) to remove all oxides and contamination.

Table 1. Composition of the substrate according to the standard.

Element	C	Mn	p	S	Fe
Content (%)	≤0.12	≤0.6	≤0.045	≤0.045	Balance

2.1.2. Coatings

Three different coatings were produced and applied on the steel substrate by the company NOF Metal Coatings Europe (NOF Metal Coatings, Creil, France). These coatings, named A, B and C, are zinc-rich films constituted of a water-based sol-gel hybrid organic–inorganic matrix, embedding metallic pigments. Ultra-pure zinc and ultra-pure aluminum lamellar particles are incorporated in this binder, as well as some corrosion inhibitors. These flakes have a diameter distribution from 5 to 30 µm.

The different compositions of the coatings are expressed in Table 2. In this study, coating A is the industrial reference. Coating B does not contain any aluminum, while coating C contains twice as much Al as coating A. These coatings were studied to consider the impact of the Al content on the corrosion. They also contain some anticorrosion inhibitors to improve their performance.

Table 2. Composition of the different coatings by percentage of total weight.

Coating	Zinc (%)	Aluminum (%)	Binder (%)	Other Pigments (%)
A	50	5	40	5
B	60	0	35	5
C	50	10	35	5

The coating materials and thickener were supplied by NOF Metal Coatings from commercial batches. The viscosity of these ready-to-use dispersions was adjusted by the addition of 0.4 wt% hydrophobically modified hydroxyethyl cellulose to achieve the appropriate viscosity for coating application. The systems were applied using a bar coating

process for all samples, with the exception of the dissolution measurements, which required plates coated on all sides. For these samples, dip coating was performed at room temperature, using a dispersion panel extraction speed of 20 mm/min. The panels were dried in an oven at 70 °C for 15 min, before being cured at 310 °C for 25 min. The final thickness of the coatings was around 5 ± 1 µm and was measured through microscope observation of cross-sections.

2.2. Dissolution Measurement

Coated panels were immersed in a 0.5 wt% NaCl aqueous solution at 50 °C. The high temperature of 50 °C was chosen to accelerate the diffusion of chemical species and to obtain a first overview of the most soluble elements in the aqueous medium. The concentration of NaCl was decreased to avoid saturating the detector. Then, in order to observe the evolution of the dissolved ions' concentration versus time, samples from the solution were collected and filtered to determine the nature and concentration of leached ions present in the electrolyte. The electrolyte samples were analyzed using inductively coupled plasma optical emission spectrometry (ICP-OES) with a Horiba JY 2000-2 (Longjumeau, France).

2.3. Electrochemical Tests
2.3.1. Open Circuit Potential

Coated panels were vertically introduced in the setup into a three-electrode system described elsewhere [42–44]. A circular area of 7.55 cm^2 was exposed to a 3 wt% NaCl aqueous solution at 30 °C. The 3 wt% solution was chosen as it has a high corrosion rate on iron and can be easily compared to the literature [5,45,46]. The open circuit potential (OCP) was measured for 1 h to ensure that the system reached electrochemical stability and obtain valid readings in the following tests. OCP was then performed at regular intervals before every other measurement to monitor the corrosion state over time. The analysis was performed via a three-electrode system using the coated sample as working electrode, a platinum net as a counter electrode and a saturated calomel electrode as a reference. A Solartron Instruments SI 1287 (Massy, France) potentiostat monitored by a personal computer via a GPIB interface and CorrWare 2.80 (Scribner Associates Inc., Southern Pines, NC, USA) software were used to run the tests and to collect the experimental data.

2.3.2. Electrochemical Impedance Spectroscopy

For electrochemical impedance spectroscopy (EIS), the same setup was used to evaluate the evolution of the electrochemical behavior of the system electrolyte/coating/substrate. The impedance response of the electrochemical system to AC excitation with a frequency ranging from 10^5 Hz to 10^{-2} Hz and peak-to-peak amplitude of 10 mV was used with a data density of 10 points per decade. AC impedance measurements were performed using a potentiostat Solartron SI 1287 and a Solartron 1255B (Massy, France) frequency response analyzer and ZPlot 2.80 (Scribner Associates Inc., Southern Pines, NC, USA) software was used to run the tests and to collect the experimental data. The impedance data were fitted with different equivalent circuits using with the simulation ZView 2.80 (Scribner Associates Inc., Southern Pines, NC, USA) equivalent circuit software [42–44]. The measurements were carried out over periods ranging from 1 h of exposure to 3 weeks. The samples were then rinsed with distilled water before other observations were made.

2.4. Normalized Tests
2.4.1. Salt Spray Test

Coated samples were submitted to accelerated corrosion tests to assess their performance. The neutral salt spray test (SST) was used for the three different systems, following the ISO 9227 norm. These tests were carried out by NOF Metal Coatings Europe (Creil, France).

2.4.2. Cross-Cut Test

The adhesion of the systems was estimated using the cross-cut test, widely used in the industry. The coatings were tested following the European norm ISO2409.

2.5. *Microstructural Characterization*

2.5.1. X-ray Diffraction

Samples' surface before and after exposure were analyzed through X-ray diffraction (XRD) to assess the formation of crystalline corrosion products. The apparatus used was a Rigaku Smartlab (Tokyo, Japan) with a Cu source. The measurement was performed at an angular speed of 10 degrees per minute, from 5 to 100 degrees, using Bragg-Brentano geometry.

2.5.2. Infrared Spectroscopy

Attenuated total reflectance Fourier-transform infrared spectroscopy (ATR-FTIR) was used to characterize the surface of the samples in order to assess the presence of typical chemical bonding due to the formation of corrosion products, even in an amorphous phase. An IS50 Spectrometer from Thermo Fisher (Waltham, MA, USA) was used and the spectra were collected from 4000 to 400 cm^{-1} with a resolution of 4 cm^{-1}.

2.5.3. Scanning Electron Microscopy

Panel specimens for cross-sectional observation were vertically embedded in resin; next polished with emery paper SiC up to 2400 then polished up to 0.25 μm using a diamond paste. The microstructure of the coatings was observed thanks to a Hitachi SU5000 (Tokyo, Japan) scanning electron microscope (SEM) using a field energy gun electron source. Energy dispersive X-ray spectroscopy (EDS) analyses were performed with a 60 mm^2 SDD detector from Oxford Instruments (Abington, UK), and the data were processed with the AZtec software (Springfield, IL, USA).

3. Results and Discussion

3.1. *Release Kinetics of Coatings Components*

Release kinetics of the coatings components were studied in 0.5 g/L NaCl solution at 50 °C by the ICP-OES technique. Samples of the electrolyte solution were taken over periods ranging from 4 h to 2 weeks of immersion to observe the evolution of the dissolved ions' concentration. Several ionic elements were detected. Zinc, silicon, and another anticorrosion (AC) pigment's content evolution over time are presented in Figure 1 for coating A and in Figures S1 and S2 for coatings B and C, respectively. Aluminum was not detected in the electrolyte for the coatings A and B. The quantity of each element found in the solution was expressed as a percentage of the total amount of that element present in the coating.

In every coating, the AC pigment was the most soluble element, with respectively 70, 50, and 40% of the element leaching into the electrolyte for coatings A, B, and C. Like the other elements, it reached a stable concentration after 48 h of immersion. This component appeared in higher proportions compared to the other elements because of the solubility of this pigment, making it easy to incorporate in the mix. This dissolution enables the chemical species to migrate to defect sites or the substrate to provide a protection.

The Si amount measured in the electrolyte was below 10% for every coating except B, in which it was around 20%. This amount did not increase after a few days, suggesting that the sol-gel matrix was not dissolving further for long immersion times. The matrix seemed to be less stable for the coating B, making it less able to retain the other elements, leading to higher amounts detected in the solution. This behavior could be explained by a catalytic effect of the Al particles on the sol-gel binder reticulation, leading to a higher cross-linking in the binder in the presence of aluminum, and a less stable matrix without the Al pigment.
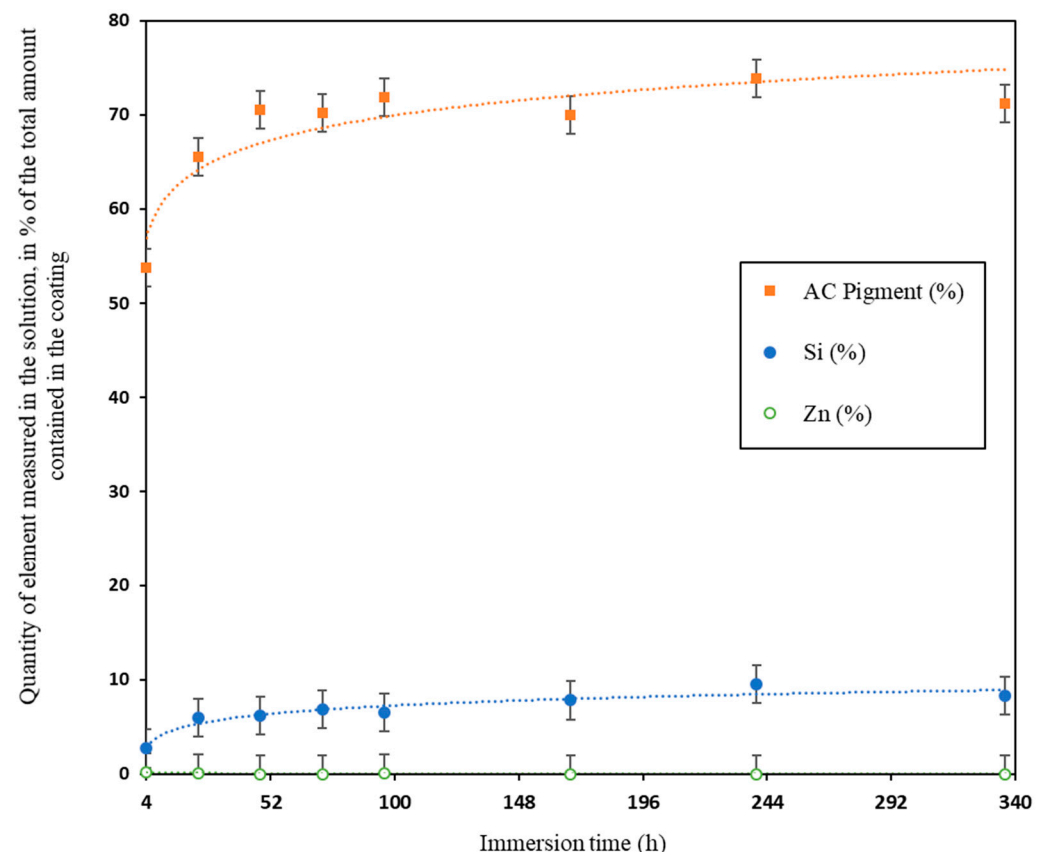
Figure 1. Evolution of the quantity of element detected by ICP-OES over immersion time for coating A.

Zn was detected in very limited quantities for every coating, at between 0.01 and 0.4%. This indicates that Zn was not diffusing in the solution during the exposure; almost the whole amount remained insoluble, in metallic or oxide form. This could be linked to the binder, which was staying cohesive enough to limit the zinc exposure to the electrolyte. The same behavior was observed for Al in coating C, with slightly higher detected quantities. For coating A, no aluminum was detected, probably due to the lower amount incorporated in this formula.

3.2. Corrosion Process Monitoring

3.2.1. OCP Study

The evolution of the open circuit potential (E_{OCP}) with time provides information about the corrosion activities of a metal interface [47,48]. Figure 2 shows the evolution of E_{OCP} when uncoated and coated substrates were immersed into the saline aqueous solution. In the case of unprotected plate, a decrease in E_{OCP} was observed after about 48 h immersion in NaCl (30 g/L). This is attributed to the dissolution of a thin oxide layer on the surface of the steel iron, followed by a slow formation of iron corrosion products such as Fe_2O_3, leading to a slight increase of potential after 72 h of immersion [49–51]. The behavior was different for the coated plates.

Concerning coated samples, for low immersion times, E_{OCP} was below -1 V$_{/SCE}$ for several hours for each formula. The first hour of immersion is not shown here as the potential was very unstable and no EIS could be performed. This corresponds to the activation period of the zinc particles. Coatings B and C followed similar paths afterward. A sharp increase in E_{OCP} values was observed after 24 h of immersion. A maximum value close to -0.6 V$_{/SCE}$ was reached after 48 h of exposure, then the E_{OCP} started decreasing and reached around -0.7 V$_{/SCE}$ after 3 weeks. On the other hand, coating A showed a different pattern from the previous one. Its E_{OCP} remained at low values for a longer period,

around 2 days. Then, it started increasing slowly in comparison to the two other coatings and reached its maximum value after 3 weeks of immersion at around -0.6 V$_{/SCE}$.
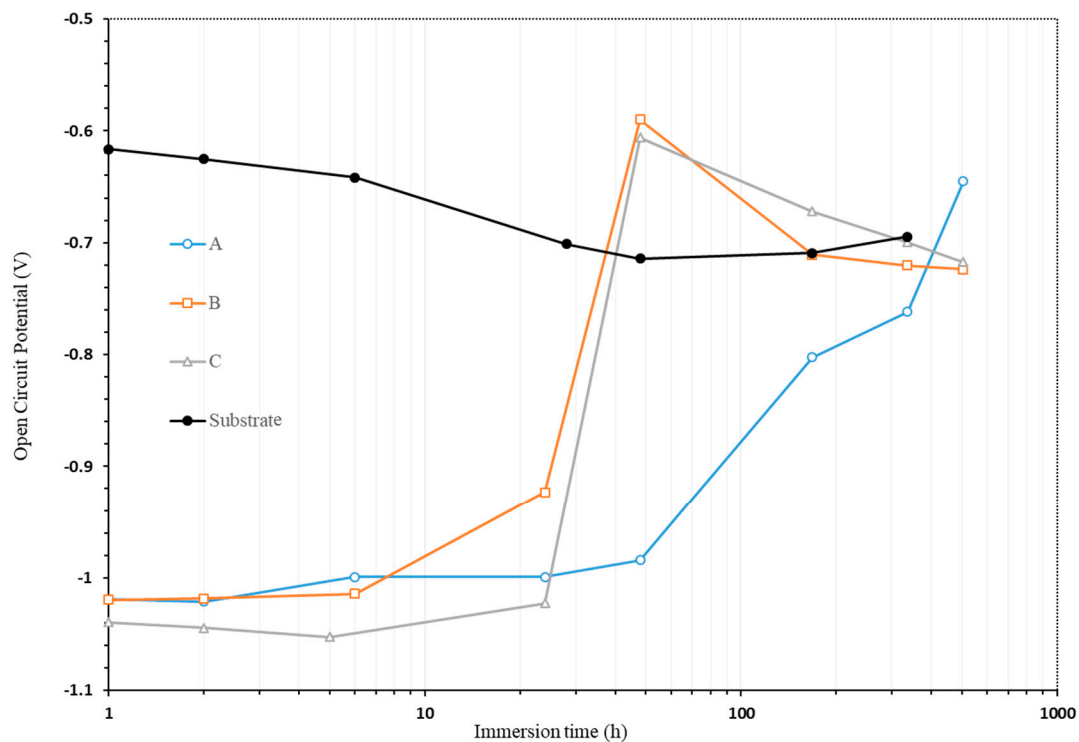

Figure 2. Evolution of the E_{OCP} over time in 3 wt% NaCl water solution.

The initial E_{OCP} of -1 V$_{/SCE}$ granted by the zinc flakes indicates that the particles were linked together and that they were electrically connected and in contact with the substrate, or at least part of the particles. This ensured that in the early immersion times, as long as the potential stayed low enough, under -0.8 V$_{/SCE}$, the cathodic protection of the steel substrate was granted [52]. For coatings B and C, the galvanic protection lasted only 24 h before fading out, while it lasted for almost a week for coating A. The increase in E_{OCP} values is due to two effects. The first one is the oxidation of zinc, leading to the formation of corrosion products with higher potential. The second one is the electrical insulation of the zinc particles, which have a lower potential than the other components of the film, from each other and from the substrate.

3.2.2. EIS Study

The corrosion behavior of coated plates in 3 wt% NaCl solution was also investigated by EIS versus time of immersion (from 1 h to 21 days) at 30 °C. Nyquist and Bode diagrams are shown in Figures 3 and 4 for coating A and Figures S3–S6 for coatings B and C, respectively. Nyquist and Bode magnitude and phase diagrams are very useful to understand the corrosion behavior of coated samples. The behavior seen in the high-frequency region in the phase plot provides information about resistance, capacitance, and water uptake of coatings, whereas the behavior seen in the low-frequency region shows the characteristic response of phenomena occurring at the metallic substrate or interface between coating and metallic substrate, as well as transport processes [37,53–55].
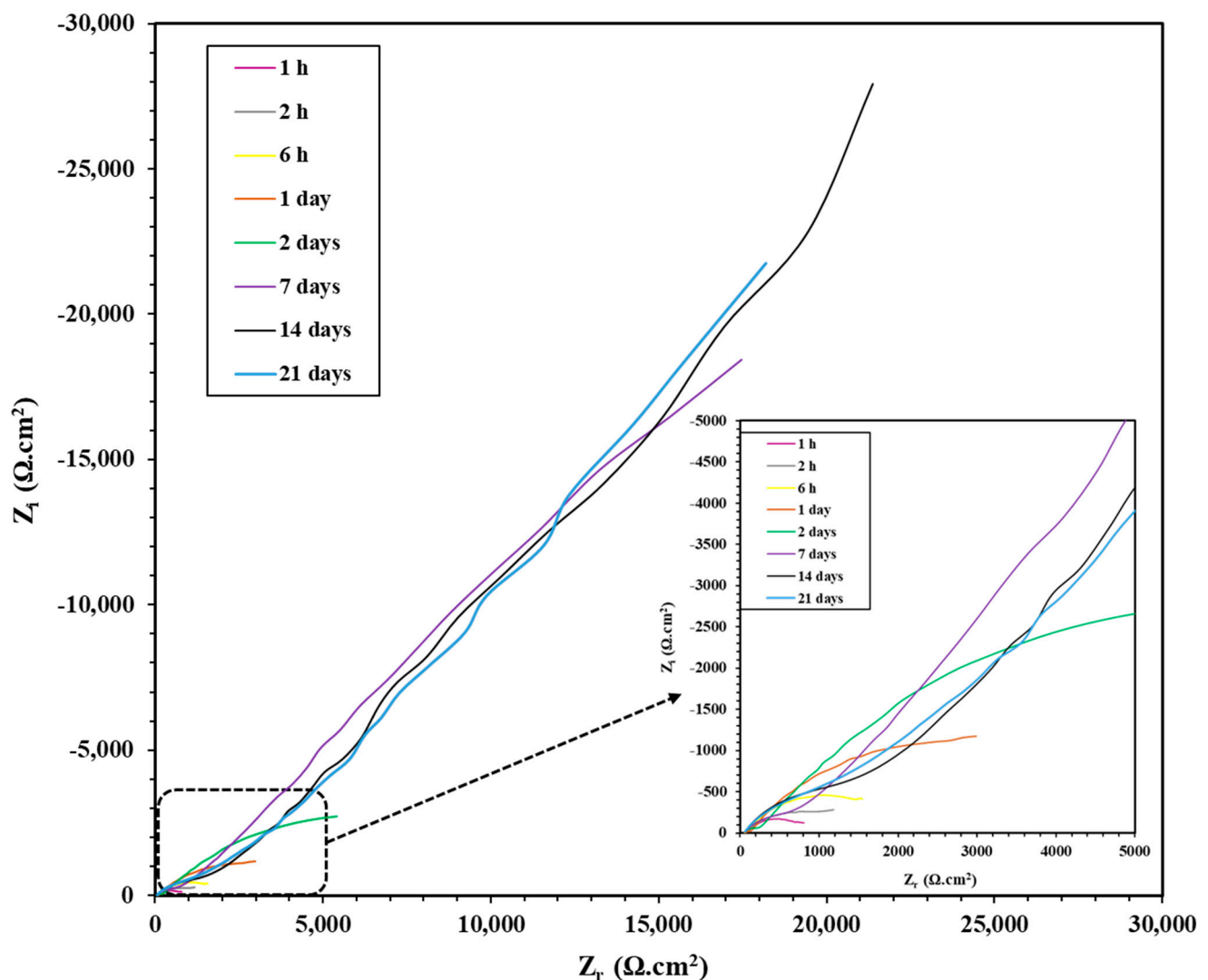
Figure 3. Nyquist diagrams of coating A during immersion time in 3 wt% NaCl water solution.

Over exposure time, the Nyquist diagram of coating A showed a change of behavior. Up to 24 h, only one semicircle was visible, whose diameter increased. After 7 days or more, another phenomenon appeared: the semicircle was followed by a semi-infinite line at an angle of 45° in the low-frequency range. Such behavior corresponds to the obvious Warburg impedance in the low-frequency region, which revealed that a diffusion-controlled corrosion process occurred due to the formation of insoluble corrosion products, blocking the mass transfer process of the corrosion reactions [7,40,46,56]. At the same time, the impedance modulus at 10^{-2} Hz increased over the immersion time, suggesting a growing global resistance of the coating [57–59]. From 1 to 6 h of immersion, the only semicircle observed on the Nyquist diagram corresponds to the only peak that appears in the phase Bode diagram in Figure 4. This shows that only one-time constant is detected at the initial state of the coating. This behavior is interpreted as the charge transfer on the metal surface, either via zinc particles connected to the steel, or on the substrate itself. After 6 h of immersion, a second semicircle and a second peak in the phase Bode diagram appeared between 10^3 Hz and 10^4 Hz. This is typical of the appearance of a barrier effect due to the formation of insoluble corrosion products in the coating defects. These products form a protective layer on the metallic pigments and substrate, slowing down the corrosion process [27,46,52]. The intensity of this peak increased over time as well, showing the progressive buildup of the protective layer. In the modulus Bode diagram, it was also possible to observe, after 2 days of immersion, a change in the slope at around 10^2 Hz,

leading to a higher modulus at frequencies above 10^2 Hz, indicating a better protective behavior. The diffusion behavior appearing after 2 days of immersion is considered to be linked to the oxygen reduction reaction, where the ingress of oxygen, as well as aggressive chloride ions, to the substrate interface is slowed by the layer of corrosion products formed through the film [5,55,60,61].
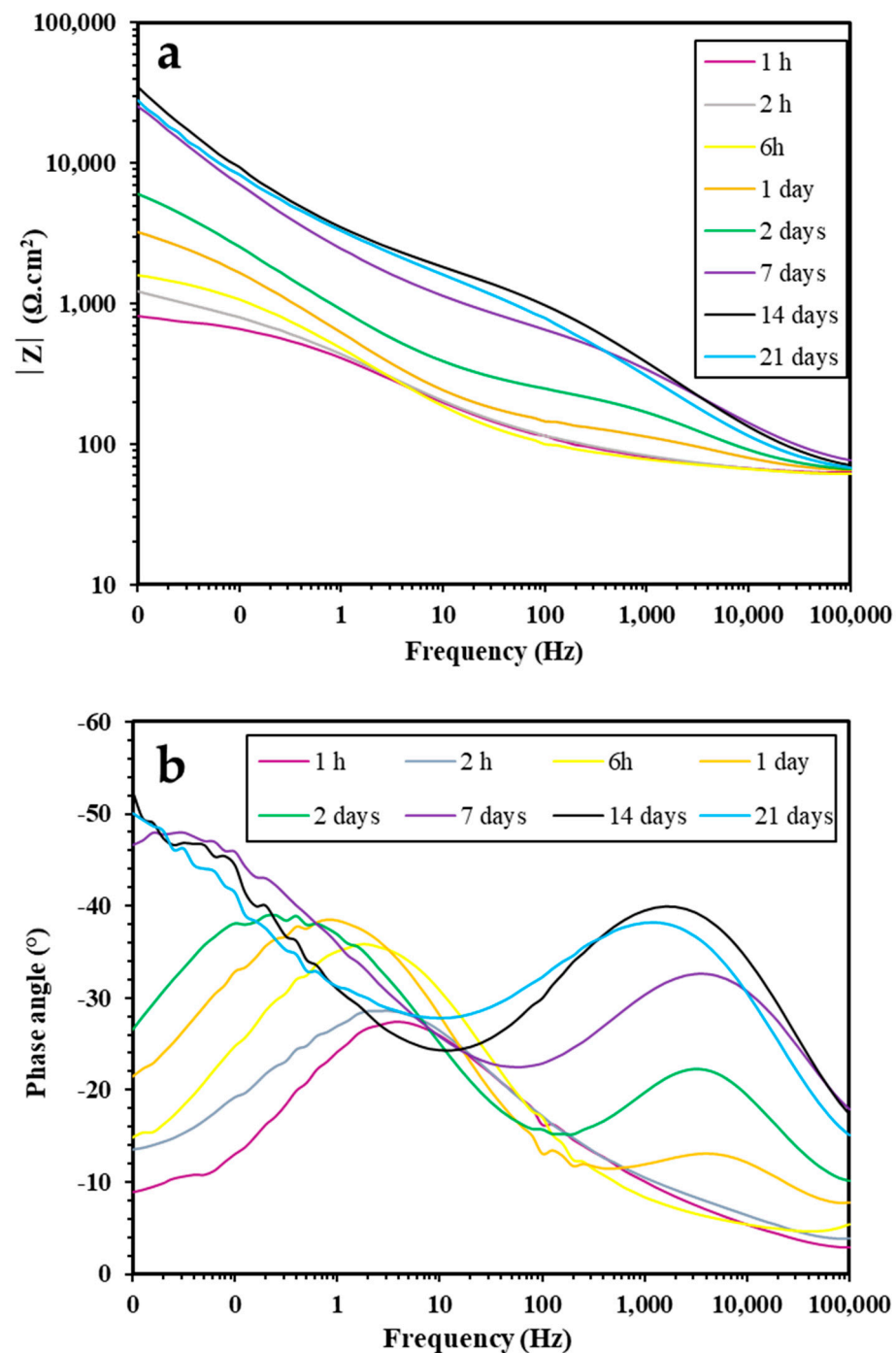

Figure 4. Bode diagrams ((**a**)—modulus and (**b**)—phase) of coating A during immersion time in 3 wt% NaCl water solution.

Coatings B and C showed a different behavior at early immersion times. Coating B exhibited only one time constant at all times, while coating C showed a second time constant for up to 6 h of exposure, then showing only one for longer durations. On other

aspects, the values reached are very similar in both Bode diagrams. The Nyquist diagrams does not show the diffusion-controlled behavior observed for coating A.

The impedance modulus at 10^{-2} Hz was specifically considered, as it gives a measure of the overall resistance of the system easily compared between each coating. As the frequency was low, all capacitive influence in the system was negligible and only the sum of all resistances remained, giving a first glimpse of the system performance [57,58,62]. The values of the impedance modulus at 10^{-2} Hz are reported in Figure 5. This implies that the corrosion products formed were not protective in the case of these coatings and did not lead to a diffusion-controlled reaction at later stages of corrosion. The second time constant observed in coating C at up to 5 h of immersion might show that this coating possesses a small barrier behavior for very short exposure durations.
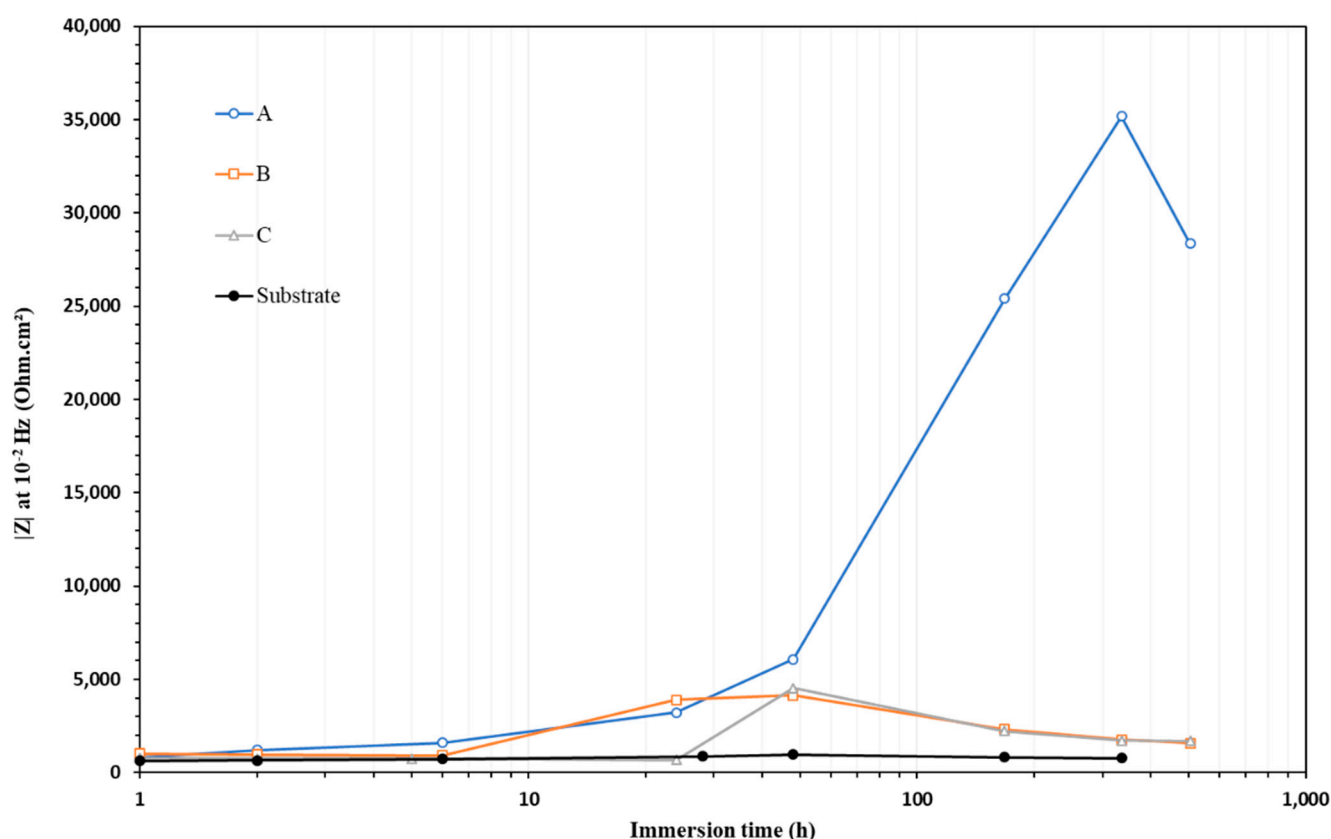

Figure 5. Evolution of the low-frequency impedance modulus over time in 3 wt% NaCl water solution.

The phase Bode diagram of coating C, containing the highest amount of Al pigments, exhibited a specific behavior, with two distinct families of peaks. From 1 h to 1 day of immersion, the peaks showed a similar intensity of around $-30°$, at a frequency of approximately 10 Hz. This is the same period where a second time constant of lower intensity was observed. From 2 to 21 days of immersion, the peak intensity reached $-50°$ at a frequency between 10^{-1} Hz and 10^{0} Hz, which was very similar to the peaks observed with coating B, which contained no Al pigment. This suggests an aluminum-dominant behavior at early immersion times, providing a low barrier effect, transitioning to a zinc-dominant behavior after 1 day of immersion where the charge transfer was not prevented anymore.

The bare substrate exhibited a modulus at 10^{-2} Hz around 6×10^{2} $\Omega \cdot cm^{2}$ for the whole immersion duration. For low immersion times, the coated samples had modulus at 10^{-2} Hz similar to the bare substrate. Coatings B and C showed again a similar behavior. Their impedance modulus at 10^{-2} Hz was low for the first hours, then slowly increased to a maximum value of 4×10^{3} $\Omega \cdot cm^{2}$ after 2 days, then decreased slowly to less than

2×10^3 $\Omega \cdot cm^2$ after 3 weeks of immersion. For coating A, the modulus at 10^{-2} Hz increased slowly for 2 days, and then increased more rapidly until 2 weeks of immersion, reaching a maximum of 3.5×10^4 $\Omega \cdot cm^2$. All coatings showed low protection at the beginning of immersion, but coating A exhibited a large increase in protective capacity for 2 weeks. At 3 weeks of exposure, its protection level started to drop.

The low modulus value at 10^{-2} Hz obtained at the beginning of the exposure shows that the film does not prevent the electrolyte from reaching the substrate or the surface of the zinc particles and does not hinder the electron transfer. This is related to the structure of the zinc-rich sol-gel coating, which is heterogeneous and porous and allows the solution to penetrate. This means that, in its initial state, the coating offers no barrier protection. During the initial period, as the electrolyte progresses through the coating, the zinc particles are being gradually wetted and start to react. This is the activation period of the zinc [5], that lasts less than 1 h because of the easy ingress of the electrolyte, with a drop of E_{OCP} that stabilizes around -1 $V_{/SCE}$. The EIS analyses were performed shortly after the activation period, as the linearity of the potential is not respected while the E_{OCP} is varying too quickly. However, as the immersion time increases, the modulus at 10^{-2} Hz increases to a greater or lesser extent depending on the coating nature. This behavior, when observed in zinc-based coatings, is generally due to the formation of corrosion products at the interface with the electrolyte. These products must be insoluble, adhesive, and thick enough to form a protective layer capable of altering the electron transfer, as observed for coating A.

To determine quantitative electrochemical parameters of the phenomenon taking place during exposure to the electrolyte, equivalent electrical circuits (EEC) were used representing the charge's path through the system components. The EIS data were fitted using two different models shown in Figure 6. Model A displayed two time constants and was used for coatings B and C at all times, as well as coating A for up to 2 days of immersion. This model is frequently used to reproduce the behavior of a coated system with electrochemical reactions at the interface [63,64]. The solution resistance was modeled by R_s and the coating resistance, or pore resistance, was represented by R_c. The capacitive behaviors were expressed using a constant phase element (CPE), instead of an ideal capacitance, to take into account the heterogeneity of the surface. The formula of the CPE impedance is:

$$Z_{CPE} = Q^{-1}(i\omega)^{-n} \tag{1}$$

where $i = \sqrt{-1}$ is the imaginary number, ω is the angular frequency in $rad \cdot s^{-1}$, Q is the CPE constant in $\Omega^{-1} \cdot s^n \cdot cm^{-2}$, and n is a factor varying from 1 in the case of an ideal capacitor behavior, to 0 in the case of an ideal resistance behavior. Using Hsu and Mansfeld's formula [65], given below, the capacitance C was calculated from the CPE parameters and parallel resistance, and is given in Table 3.

$$C = \left(QR^{1-n}\right)^{\frac{1}{n}} \tag{2}$$

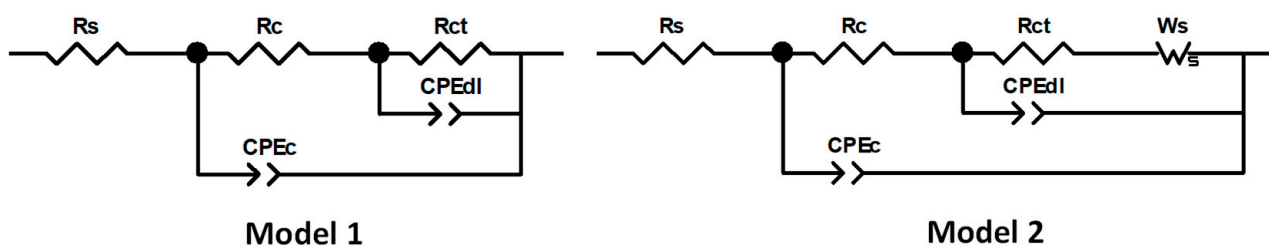**Model 1**　　　　　　　　　　　　　　　　　　**Model 2**

Figure 6. Equivalent electrical circuits used to fit the EIS data of the coating A at early immersion times and coatings B and C at all times (model 1) and to fit coating A at later immersion times (model 2).

Table 3. Values of EIS parameters of coating A versus immersion time in 3 wt% NaCl.

Time	R_s ($\Omega \cdot cm^2$)	R_c ($\Omega \cdot cm^2$)	C_c ($F \cdot cm^{-2}$)	n_c	R_{ct} ($\Omega \cdot cm^2$)	C_{dl} ($F \cdot cm^{-2}$)	n_{dl}	Ws-R ($\Omega \cdot cm^2$)	Ws-T (s)	Ws-P	χ^2
1 h	59	181	5.82×10^{-5}	0.44	701	4.77×10^{-5}	0.77	-	-	-	6×10^{-4}
2 h	56	190	6.21×10^{-5}	0.39	1458	4.10×10^{-5}	0.77	-	-	-	3×10^{-4}
6 h	55	48	3.97×10^{-6}	0.43	2098	2.03×10^{-4}	0.66	-	-	-	7×10^{-4}
24 h	58	72	6.87×10^{-7}	0.63	4490	1.29×10^{-3}	0.57	-	-	-	6×10^{-4}
48 h	59	183	6.71×10^{-7}	0.64	11544	1.72×10^{-3}	0.55	-	-	-	2×10^{-4}
7 days	53	749	6.10×10^{-7}	0.57	5373	1.13×10^{-4}	0.55	158,210	24.39	0.60	7×10^{-5}
14 days	51	1712	1.07×10^{-6}	0.60	1607	1.74×10^{-5}	0.68	93,923	59.69	0.55	3×10^{-4}
21 days	52	1459	1.61×10^{-6}	0.59	5064	4.76×10^{-5}	0.57	121,580	54.33	0.59	1×10^{-4}

The film global capacitive response was modeled by CPE$_c$, and the charge transfer resistance, representing the low-frequency resistive behavior of the coating owing to the electrical charges passing from the electrolyte to the substrate, was simulated by R_{ct}. The double-layer capacitance, referring to the adsorbed molecule layer at the interface between coating and substrate inducing a capacitive behavior, was represented by CPE$_{dl}$. This was similar in model B to that in model A but contained an additional Warburg element W_s, which accounts for the diffusional phenomena witnessed at longer immersion times.

The values of the different components of the circuits used to model coating A are reported in Table 3. The typical examples of the fitted Nyquist diagrams with the used EEC models (model 1 and model 2), described in Figure 6, are presented in Figure S7 (see Supplementary Materials). The accuracy of the EIS measurements can be verified from the strong agreement between the experimental plots and fitting lines (Figure S7), as well as the values of goodness of fit in Table 3. Indeed, the goodness of fit chi-squared (χ^2) values are of the order of 10^{-4} (Table 3), suggesting the validity of the proposed circuits (in theory, the lower value of χ^2 shows that the fitted data agree well with the experimental data).

From the obtained results in Table 3, it is observed that the coating's resistance R_c was initially very low and increased up to 14 days and followed the same pattern as the modulus. At the same time, the capacitance C_c decreased up to 14 days. R_{ct} increased up to 48 h of immersion, then went down when the fitting model changed, while W_s-R was very high, around 10^5 $\Omega \cdot cm^2$, for 7, 14, and 21 days of immersion.

The values of R_s stayed stable over the immersion period, varying from 51 to 59 $\Omega \cdot cm^2$. These values are in the same order of magnitude as the ones found in the literature [5,42,46,66]. The simultaneous increase of R_c and decrease of C_c from 6 h to 14 days indicates a stronger barrier effect, confirming the formation of an insoluble corrosion products layer. That R_c was slightly higher at 1 h and 2 h of immersion may be due to an activation period of the zinc particles where the charge transfer is not completely installed yet. The initial increase of R_{ct} is also a sign that electrochemical reactions taking place at the interface between electrolyte and Zn flakes or steel surface are being slowed down. At 7 days, the Warburg parameter W_s-R reached very high values at 1.58×10^5 $\Omega \cdot cm^2$, 30 times higher than R_{ct}, which shows a very strong influence of the diffusion of chemical species over the whole electrochemical response of the coating. Considering these parameters, it seems that the protection offered by coating A was obtained through limitation of the diffusion of the reactive species towards the interface, more than slowing down the charge transfer at the interface. These EEC parameters seemed to be in the same order of magnitude as those found in some inorganic ZRC [67,68].

The values obtained after fitting for the different coatings were compared at 2 h and 14 days of immersion, as displayed in Table 4. Coating B had a lower coating resistance R_c, 20 $\Omega \cdot cm^2$, compared to coating A, but quite similar values otherwise at 2 h of immersion. After 2 weeks, it still had a very low R_c, a quite high C_c, and a very low n_c coefficient. Its R_{ct} was slightly higher, at 3920 $\Omega \cdot cm^2$, but still in the same order of magnitude as the other coatings. However, the C_{dl} of coating B was higher than that of the others, but with the lowest n_{dl} of the three. All this suggests that it had the lowest barrier effect of the three

coatings, leading to a very degraded coating at 2 weeks, with almost no protection granted by the remaining binder, as shown by the low R_c. For the coating C at early immersion time, it was observed that it had slightly lower C_c values and higher R_c and n_c coefficients, meaning a more capacitive behavior than the other coatings, but a much lower R_{ct} and higher C_{dl} than A and B, indicating an easier zinc reaction with the electrolyte, maybe due to a higher active surface area of zinc [23]. For longer immersion durations, it had a lower R_c and a higher C_c than the other systems. This indicates that the binder was not protecting the substrate anymore and no protection was granted by the corrosion product layer.

Table 4. Comparison of the fitting parameters for the three coatings at 2 h and 14 days of immersion time in 3 wt% NaCl water solution.

Time	Coating	R_s ($\Omega \cdot cm^2$)	R_c ($\Omega \cdot cm^2$)	C_c ($F \cdot cm^{-2}$)	n_c	R_{ct} ($\Omega \cdot cm^2$)	C_{dl} ($F \cdot cm^{-2}$)	n_{dl}	Ws-R ($\Omega \cdot cm^2$)	Ws-T (s)	Ws-P	χ^2
	A	56	190	6.21×10^{-5}	0.39	1458	4.10×10^{-5}	0.77	-	-	-	3×10^{-4}
2 h	B	58	20	1.16×10^{-5}	0.46	1214	4.25×10^{-4}	0.74	-	-	-	7×10^{-4}
	C	59	567	2.86×10^{-4}	0.63	262	2.96×10^{-2}	0.78	-	-	-	1×10^{-3}
	A	51	1712	1.07×10^{-6}	0.60	1607	1.74×10^{-5}	0.68	93,923	59.69	0.55	3×10^{-4}
14 days	B	44	11	1.46×10^{-8}	0.35	3920	3.77×10^{-3}	0.61	-	-	-	2×10^{-4}
	C	56	286	1.43×10^{-3}	0.66	2357	1.66×10^{-4}	0.98	-	-	-	1×10^{-3}

After 2 weeks of exposure, R_{ct} values were quite similar in the different coatings, even though the corrosion protection granted by coating A was much stronger. However, R_c at 14 days of immersion it was higher for coating A, showing that the film was granting a better barrier effect. When comparing this value, at 1712 $\Omega \cdot cm^2$, with the Ws-R value, at 93,923 $\Omega \cdot cm^2$, it seems that the Warburg element was providing the strongest effect in the system, which seems to be consistent with the Nyquist diagram exhibiting a long tail in the low-frequency region, with a much higher dimension compared to the observable semicircle attributed to the charge transfer and barrier effect. This suggests that the main contribution to coating A's anticorrosion properties came from the diffusive behavior.

3.2.3. Optical Observation

After 3 weeks of immersion, the samples were removed from the solution and rinsed with distilled water, then dried. As presented in Figure 7, some coatings were more corroded than the others.
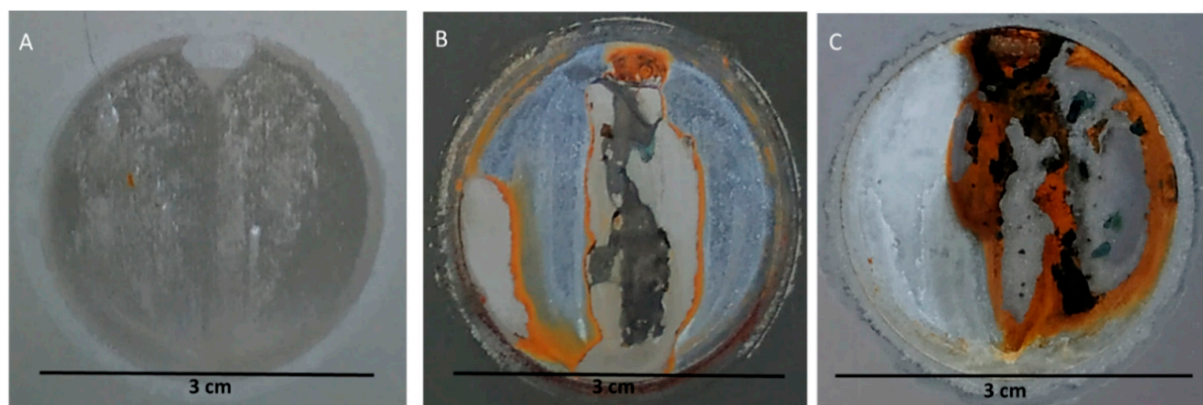

Figure 7. Surface of the coatings after 3 weeks of immersion in 3 wt% NaCl water solution. (**A**)—coating A, (**B**)—coating B and (**C**)—coating C.

Coatings B and C both exhibited a very degraded surface, with some red rust and some delamination, as well as grey corrosion products. Coating A presented very few signs of degradation. Almost only gray rust was visible, with a very small spot of red rust but no delamination. Coating A provided the best protection for 3 weeks of immersion,

while B and C did not protect the substrate for the whole duration. This corroborates the results found through electrochemistry, as both the OCP and the impedance suggested that coatings B and C did not protect the substrate after a few days of exposure.

The neutral SST evaluations performed by the company following the ISO 9227 norm show globally the same ranking of the coatings. Coating A showed no sign of red rust for more than 1500 h, B for 1000 h, and C for 500 h. The adhesion of the coating before exposure was also tested following the ISO2409 standard, and results are shown in Table 5. All systems showed good adhesion results.

Table 5. SST, aspect description, and adhesion rating of the coatings.

Coating	SST (h)	Aspect after 21 Days of Immersion	Adhesion
A	1500	White-gray	0
B	1000	Gray and red rust	0
C	500	White-gray and red rust	0

As coating A showed the highest performance in electrochemical properties and corrosion protection, the rest of the characterizations were more focused on this specific formula to understand the mechanisms of this protection.

3.3. Microstructural Characterization

3.3.1. XRD Study

Ccoating A was characterized through XRD before and after the exposure to assess the formation of crystalline corrosion products. Samples immersed for 2 days, 1 week, and 3 weeks were analyzed, and the results are presented in Figure 8 with relative intensities for comparison purposes.
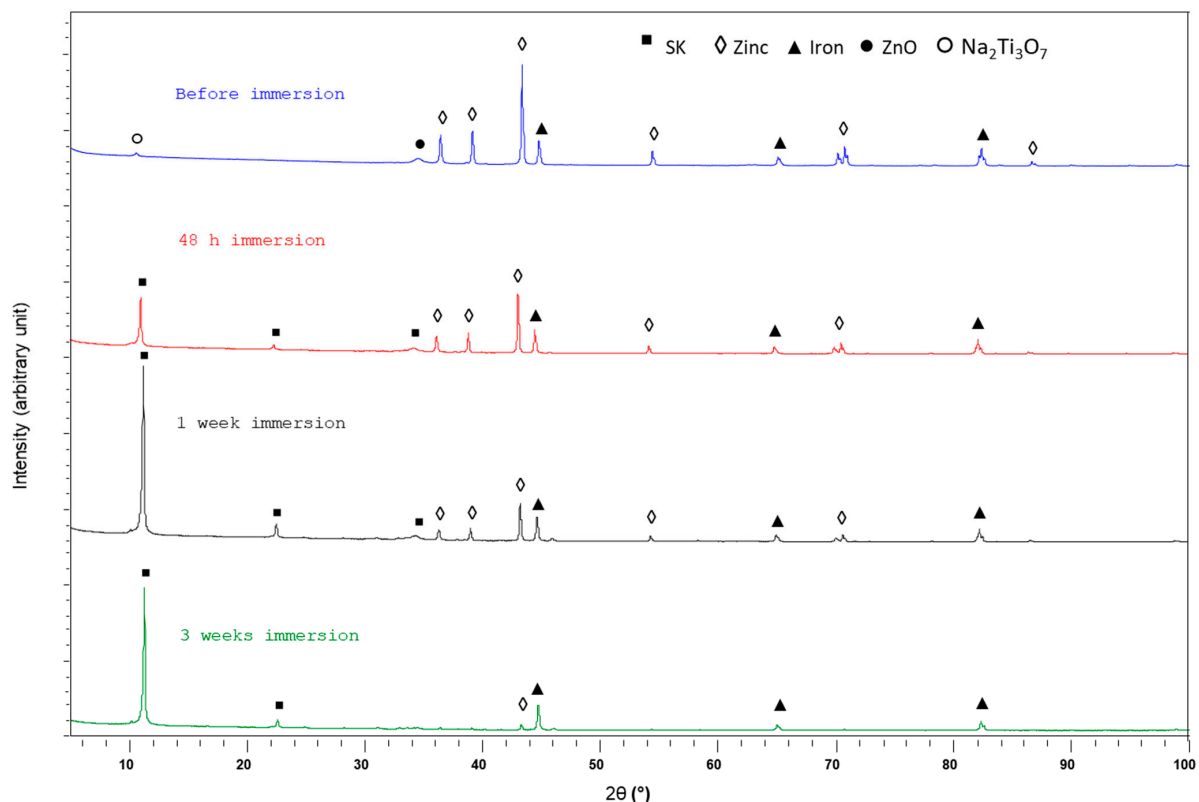

Figure 8. Diffractograms of the surface of coating A, before and after different durations of exposure in 3 wt% NaCl water solution.

Before immersion, metallic zinc (PDF 04-0831) and iron (PDF 06-0696) were detected, as well as zincite ZnO (PDF 36-1451). Traces of sodium titanium oxide $Na_2Ti_3O_7$ (PDF 00-031-1329) were also found but disappeared after the immersion. After 48 h of immersion, specific peaks of simonkolleite (SK) $Zn_5(OH)_8Cl_2 \cdot H_2O$ (PDF 76-0922) appeared. SK is a very common corrosion product of zinc in chloride environments [26,52,69,70]. The peaks specific for (003) and (006) crystallographic planes had a much higher intensity than the other characteristic peaks of SK. The small peak detected at $10°$ is not the same as SK, it indicates the presence of sodium titanium oxide, which is compatible with the elements in the binder. It was not visible after the immersion due to the superposition of the peaks. The same happened with ZnO peaks, so it is difficult to assess its presence after exposure. At the same time, the intensity of the Zn peak decreased. After 1 week, the SK peaks were more intense while the pure Zn peaks became lower. At 3 weeks of exposure, the SK peaks decreased slightly in intensity and the Zn peaks almost disappeared completely. Iron was detected through the whole experiment. The XRD data show that zinc was reacting during the immersion, and that SK was forming for at least 1 week.

A comparison between the three coatings after exposure is shown in Figure 7, show that SK was present in the three coatings, with higher amounts in coating A but lower amounts in coating B. The higher intensity of peaks (003) and (006) are due to a specific orientation of the crystal, as SK grows in sheet structure, inducing a preferred orientation of the crystals. The metallic zinc seemed completely consumed in coating C and almost consumed in coating B. Coating B also showed some traces of ZnO, while coating C exhibited signs of layered double hydroxide (LDH) $Zn_{0.7}Al_{0.3}(OH)_2(CO_3)_{0.15} \cdot xH_2O$ (PDF 00-048-1022), whose peaks partially overlapped with SK. Some peaks specific to a corrosion product of iron, lepidocrocite γ-FeO(OH), were also found in coating C.

The initial detection of zincite was due to the formation ZnO on the surface of the flakes during the production process. The formation of SK and its increasing amount over time follows the evolution of the impedance modulus at low frequency, which suggests that this corrosion product is responsible for the formation of a protective layer [69,71]. It can be noted that no iron corrosion products were detected on coating A; only the metallic Fe was found, which confirms that the substrate was not corroding after 3 weeks of immersion, as can be seen from the optical observations. Coating B showed no iron corrosion products either, even though the optical observation demonstrated the formation of red rust. Coating C, however, presented peaks of lepidocrocite γ-FeO(OH) (PDF 44-1415) which are consistent with the rusting of the substrate. The formation of Zn-Al LDH in the coating C may be due to the higher amount of aluminum and more advanced state of corrosion leading to favorable pH conditions for alumina dissolution and formation of aluminum ions [72,73]. When comparing the metallic zinc remaining after the corrosion, it appears that coating A had the highest amount of still unoxidized zinc, while the zinc flakes in coating B were almost completely consumed and no metallic zinc was detected in coating C after 3 weeks of immersion. This confirms that zinc was more active in coating C and was completely consumed before the end of the experiment, supporting the electrochemical observations suggesting that reactions taking place in coating C at early immersion times were facilitated.

3.3.2. FTIR Study

To detect corrosion products formed and confirm the ones already detected, ATR-FTIR was performed on the coatings, before and after immersion in the NaCl solution and the spectra obtained are shown in Figures S9–S11.

Before exposure, only one band was observed, in the case of coatings A and B, between 1050 and 1150 cm^{-1}. This band is linked to the stretching vibrations of the Si-O-Si bonds [21,44,74,75]. This shows that the sol-gel matrix formed a strong network during the condensation reaction. However, this band was not observed in coating C. This might be due to the higher load in Al, which induced a higher reflective power at the surface of the film.

After exposure, coating A and B showed almost the same absorption bands. Around 1580 cm^{-1} and 1400 cm^{-1}, these bands indicated the formation of carbonate, generally associated with hydrozincite (HZ) $Zn_5(OH)_6(CO_3)_2$ [8,76–78]. Some other bands, found at 1050 cm^{-1}, 890 cm^{-1}, and 710 cm^{-1} are linked to the presence of SK [76,78]. Some of the peaks characteristic of HZ may also overlap with ones typical of SK. These results combined with XRD confirm that SK was indeed created during the corrosion process but also show that HZ was present too in the coating, but in an amorphous state.

The FTIR spectrum of coating C exhibited a different profile, with more defined peaks and only a few wide bands. A broad band at 3400 cm^{-1} is a sign of O-H bonds, linked to the presence of H_2O still inside the coating [78–80]. The band found at 1580 cm^{-1} is also a sign of the formation of HZ, as well as the peak at 1360 cm^{-1}. This peak, which partly covered the band that is expected at 1400 cm^{-1}, is specific to (LDH) $Zn_2Al(OH)_6(CO_3)_{1/2} \cdot xH_2O$, which matches the LDH detected in this coating by XRD. The following peaks at 770 cm^{-1}, 610 cm^{-1}, 550 cm^{-1}, and 430 cm^{-1} were also due to LDH [76,81,82]. The fact that these peaks were quite sharp is the consequence of the crystallinity of LDH. This compound was in a hydrated state, which explains the presence of the band specific to H_2O presence only in this coating.

3.3.3. SEM and EDS Studies

The coatings were observed before exposure and after 21 days of immersion. Observation of the cross-section of the non-corroded coating A with secondary electrons (SE) and backscattered electrons (BSE) is presented in Figure 9. The lamellar structure of the coating was evidenced, with some different kinds of flake visible as well as some cracks in the binder.
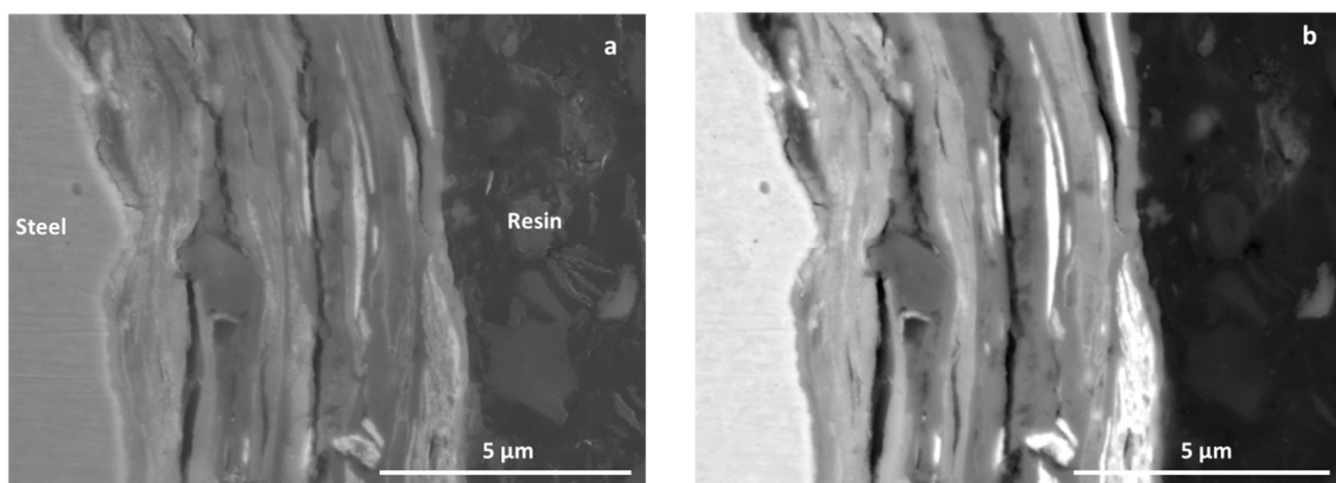

Figure 9. SE (**a**) and BSE (**b**) picture of coating A before immersion in 3 wt% NaCl water solution.

The elemental mapping in Figure 10 shows that zinc and aluminum flakes were clearly defined, as well as the silicon matrix. The Si mapping demonstrates that the matrix was indeed embedding the different metallic flakes together.

The lamellar microstructure of the coating was similar after 3 weeks of immersion, as shown in Figure 11. The main changes can be observed through the EDX mapping in Figure 12. Chlorine was now clearly visible on the cross-section and was localized on the zinc flakes, but not on the substrate. No chlorine was detected in the non-exposed sample. Zinc was now present through the whole thickness instead of being found exclusively on the flakes. In contrast, aluminum and silicon were still clearly localized.
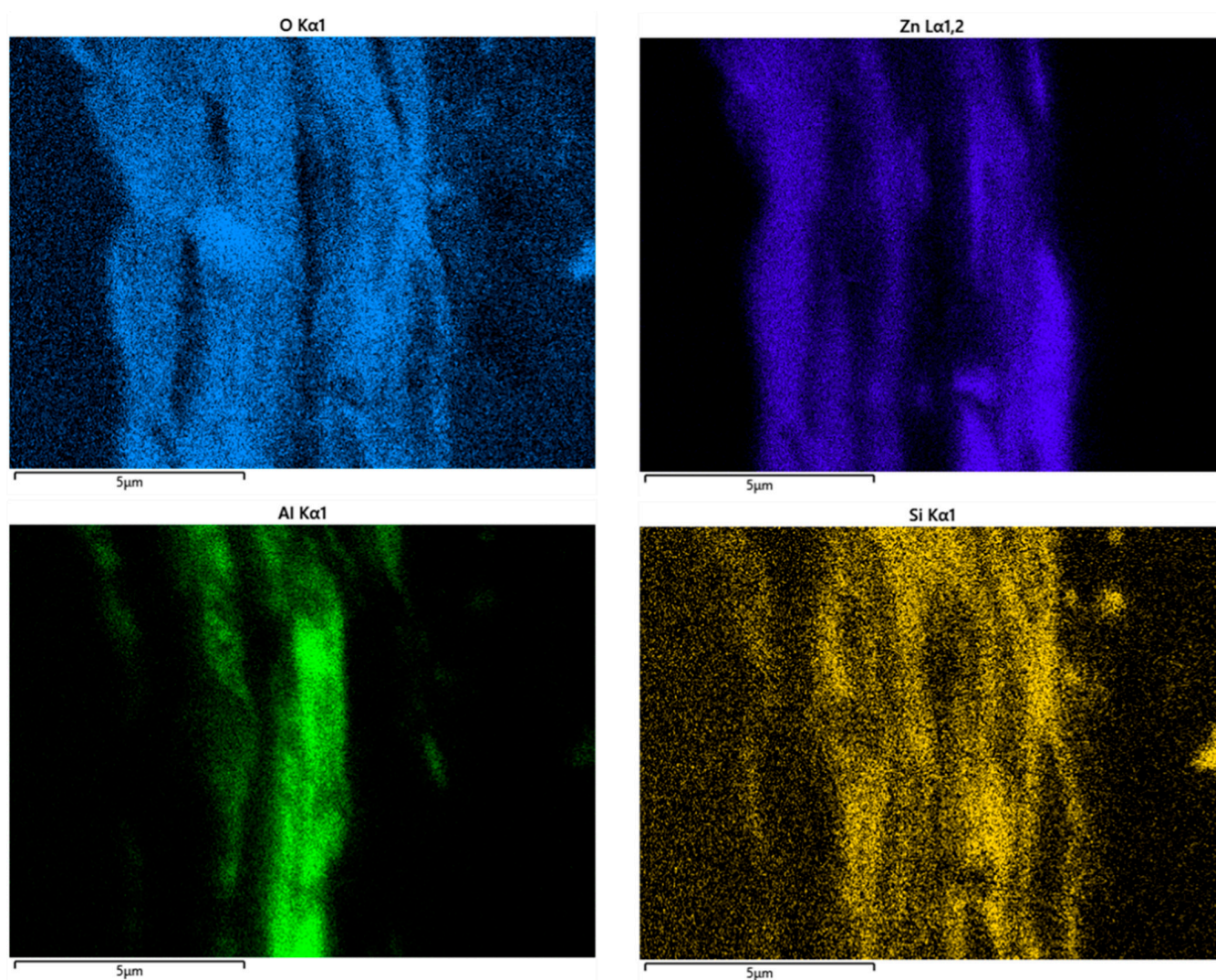
Figure 10. EDX mapping of O, Zn, Al, and Si in the cross-section of an unexposed coating A sample.
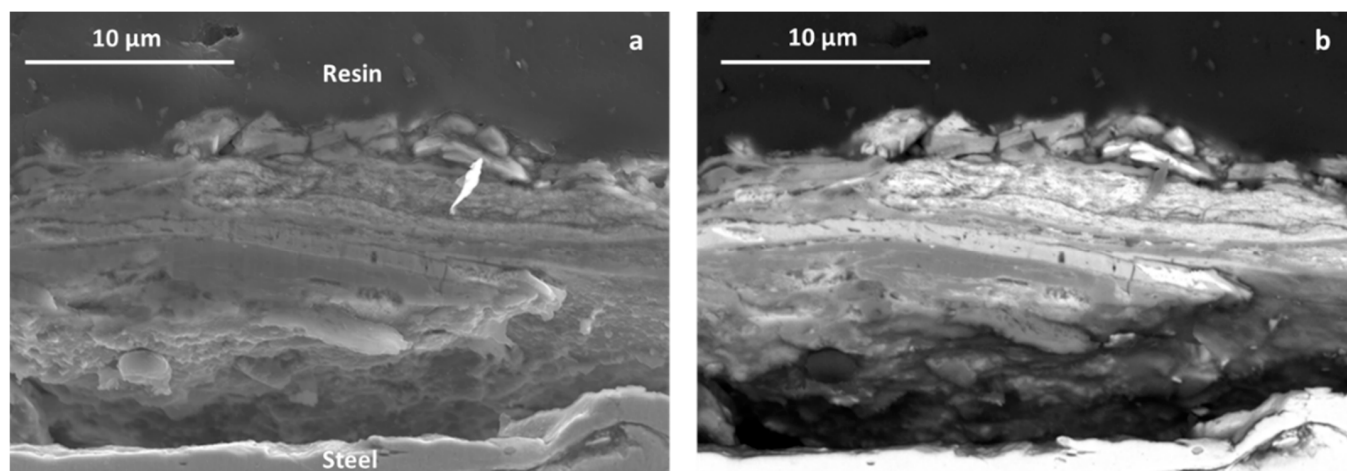

Figure 11. SE (**a**) and BSE (**b**) picture of coating A after immersion in 3 wt% NaCl water solution.
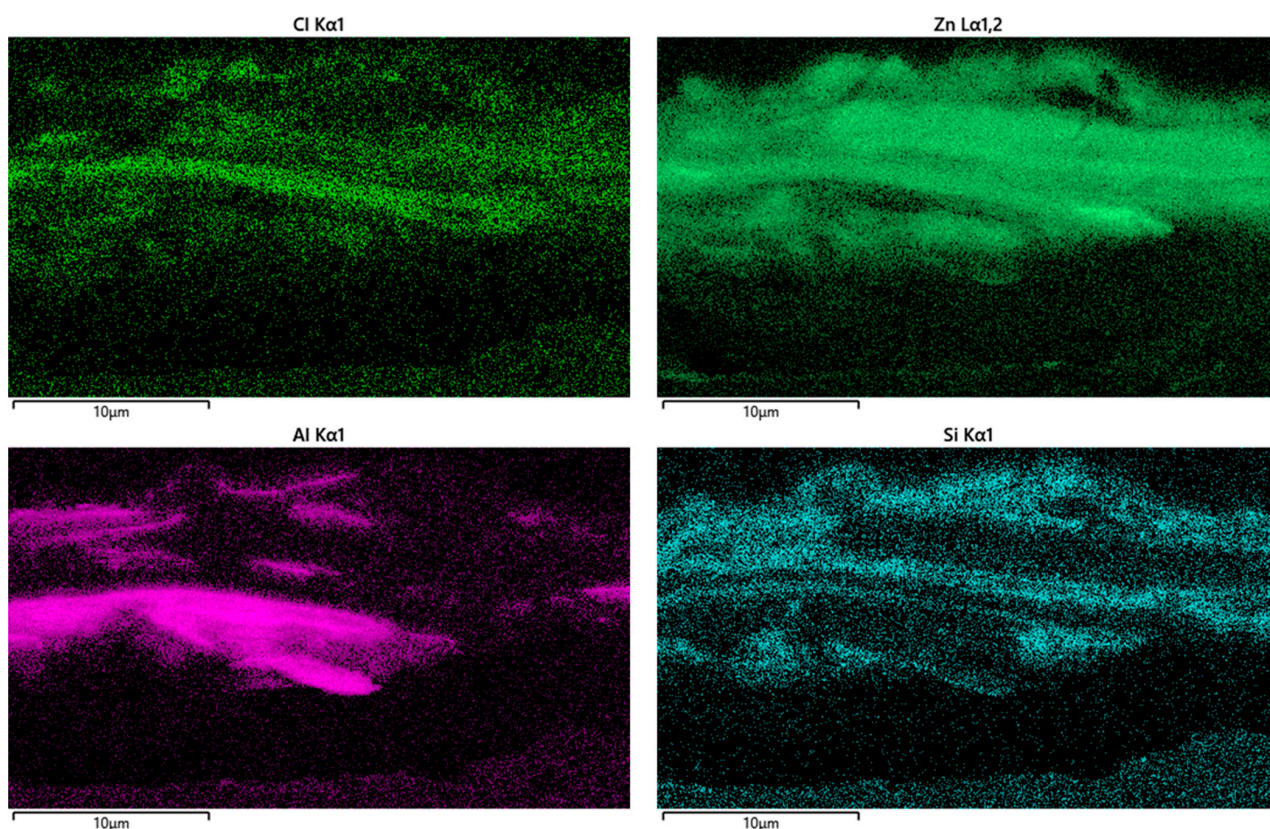
Figure 12. EDX mapping on the cross-section of a coating A sample after immersion in 3 wt% NaCl water solution.

The proportions of chlorine, zinc, and oxygen were measured by EDX and the resulting spectrum is given in Figure 13. The proportions obtained match the theoretical one of the simonkolleite, confirming the XRD results.
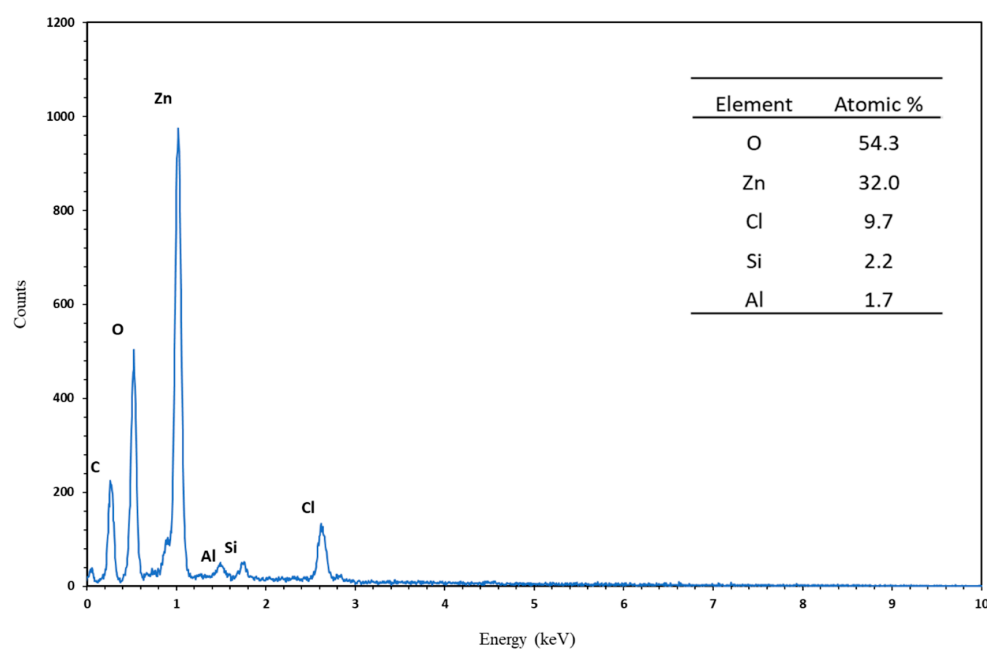

Element	Atomic %
O	54.3
Zn	32.0
Cl	9.7
Si	2.2
Al	1.7

Figure 13. EDX spectrum of coating A after immersion in 3 wt% NaCl water solution, on the high-chloride concentration zone.

The small peaks of silicon and aluminum are in accordance with the very low amount detected in solution by ICP, suggesting a very low reactivity of these elements. The absence of chlorine on the steel indicates that the substrate was protected by the coating and was not attacked by the NaCl solution. The Cl ions were bound to zinc particles, where partial dissolution of the flakes occurred, forming some crystalline corrosion products on the flake: simonkolleite. When chloride ions ingressed through the coating, they reacted with the flakes and could not reach the substrate. At other locations in the coating, higher or lower concentration of chlorine were detected and sometimes no chlorine at all. In places without Cl, other corrosion products were observed through low Zn concentration out of the lamellae, which may be hydrozincite, as it is composed only of Zn, O, C, and H.

4. Conclusions

Waterborne hybrid sol-gel coatings with different aluminum flake contents were tested for corrosion resistance. It was shown that two different behaviors may occur. Coatings B and C, with respectively 0 and 10% Al, degraded more rapidly with the formation of red rust, which was confirmed by the electrochemical tests. Coating A, with 5% of Al, performed the best results in terms of corrosion resistance, which was evidenced by low OCP values for longer durations and a sharp increase in impedance modulus at 10^{-2} Hz after 2 days of immersion.

The protective behavior of coating A at early immersion stage was due to the low potential of zinc providing galvanic protection to the steel, as no barrier effect from the film was observed. Over time, zinc was consumed and the potential gradually increased. Zinc was no longer able to provide cathodic protection, but reacted with the electrolyte, leading to the formation of corrosion products able to hinder the diffusion of aggressive species to the substrate, therefore slowing down the corrosion.

The lack of aluminum flakes in coating B influenced the properties of the binder, which degraded faster and failed to correctly retain all of the anticorrosion pigments. In contrast, in coating C, if the Al pigment amount was too high, corrosion products such as simonkolleite and amorphous hydrozincite as well as LDH formed, but without granting protective properties to the coating. The total consumption of Zn in C coating is a sign of increased reactivity of the zinc flakes when the aluminum content is too high. This increases the effect of local concentration and pH changes that occur in the coating during corrosion, preventing the formation of dense layers.

Supplementary Materials: The following supporting information can be downloaded at: https://www.mdpi.com/article/10.3390/coatings12101390/s1, Figure S1: Evolution of the quantity of element detected by ICP-OES over immersion time for coating B, Figure S2: Evolution of the quantity of element detected by ICP-OES over immersion time for coating C, Figure S3: Nyquist diagrams of the coating B during immersion time in 3 wt% NaCl water solution, Figure S4: Bode ((**a**) Modulus and (**b**) Phase) diagrams of the coating B during immersion time in 3 wt% NaCl water solution, Figure S5: Nyquist diagrams of the coating C during immersion time in 3 wt% NaCl water solution, Figure S6: Bode (Modulus (**a**) and Phase (**b**)) diagrams of the coating C during immersion time in 3 wt% NaCl water solution, Figure S7: Nyquist diagrams of coating A after 2 h of immersion fitted with model 1 (a) and after 14 days of immersion fitted with model 2 (b), Figure S8: Diffractograms of the surface of coatings A, B and C after 21 days of exposure in 3 wt% NaCl water solution, Figure S9: ATR-FTIR spectra of the coating A before and after exposure to 3 wt% NaCl water solution, Figure S10: ATR-FTIR spectra of the coating B before and after exposure to 3 wt% NaCl water solution, Figure S11: ATR-FTIR spectra of the coating C before and after exposure to 3 wt% NaCl water solution.

Author Contributions: Conceptualization, A.B.; Funding acquisition, F.G.; Investigation, J.-B.V.; Methodology, A.B., F.B. and J.-B.V.; Project administration, J.-B.V.; Supervision, F.G. and J.-B.V.; Writing—original draft, A.B.; Writing—review and editing, C.J. All authors have read and agreed to the published version of the manuscript.

Institutional Review Board Statement: Not applicable.

Informed Consent Statement: Not applicable.

Data Availability Statement: Data sharing is not applicable to this article.

Conflicts of Interest: The authors declare no conflict of interest.

References

1. Mudd, G.M.; Jowitt, S.M.; Werner, T.T. The World's Lead-Zinc Mineral Resources: Scarcity, Data, Issues and Opportunities. *Ore Geol. Rev.* **2017**, *80*, 1160–1190. [CrossRef]
2. Sverdrup, H.U.; Olafsdottir, A.H.; Ragnarsdottir, K.V. On the Long-Term Sustainability of Copper, Zinc and Lead Supply, Using a System Dynamics Model. *Resour. Conserv. Recycl. X* **2019**, *4*, 100007. [CrossRef]
3. Morcillo, M.; Barajas, R.; Feliu, S.; Bastidas, J.M. A SEM Study on the Galvanic Protection of Zinc-Rich Paints. *J. Mater. Sci.* **1990**, *25*, 2441–2446. [CrossRef]
4. Sørensen, P.A.; Kiil, S.; Dam-Johansen, K.; Weinell, C.E. Anticorrosive Coatings: A Review. *J. Coat. Technol. Res.* **2009**, *6*, 135–176. [CrossRef]
5. Abreu, C.M.; Izquierdo, M.; Keddam, M.; Nóvoa, X.R.; Takenouti, H. Electrochemical Behaviour of Zinc-Rich Epoxy Paints in 3% NaCl Solution. *Electrochim. Acta* **1996**, *41*, 2405–2415. [CrossRef]
6. Park, J.H.; Yun, T.H.; Kim, K.Y.; Song, Y.K.; Park, J.M. The Improvement of Anticorrosion Properties of Zinc-Rich Organic Coating by Incorporating Surface-Modified Zinc Particle. *Prog. Org. Coat.* **2012**, *74*, 25–35. [CrossRef]
7. Feliu, S.; Barajas, R.; Bastidas, J.; Morcillo, M.; Feliu, S. Study of Protection Mechanisms of Zinc-Rich Paints by Electrochemical Impedance Spectroscopy. In *Electrochemical Impedance: Analysis and Interpretation*; ASTM International: West Conshohocken, PA, USA, 1993; p. 438.
8. Nagasawa, M.; Okada, N.; Otsuka, N.; Ohtsuka, T. Corrosion Process of Inorganic Zinc-Rich Painted Steel Exposed to a High-Chloride Atmospheric Environment. *ISIJ Int.* **2018**, *58*, 316–322. [CrossRef]
9. Barton, K.; Cullen, M.; Duffy, B. Sol-Gel Chemistry Engineering for Corrosion Protection. In *Sol-Gel Materials for Energy, Environment and Electronic Applications*; Pillai, S.C., Hehir, S., Eds.; Advances in Sol-Gel Derived Materials and Technologies; Springer International Publishing: Berlin/Heidelberg, Germany, 2017.
10. Wang, D.; Bierwagen, G.P. Sol-Gel Coatings on Metals for Corrosion Protection. *Prog. Org. Coat.* **2009**, *64*, 327–338. [CrossRef]
11. Wang, X.; Xing, W.; Song, L.; Yang, H.; Hu, Y.; Yeoh, G.H. Fabrication and Characterization of Graphene-Reinforced Waterborne Polyurethane Nanocomposite Coatings by the Sol-Gel Method. *Surf. Coat. Technol.* **2012**, *206*, 4778–4784. [CrossRef]
12. Wint, N.; Wijesinghe, S.L.; Yan, W.; Ong, W.K.; Wu, L.Y.; Williams, G.; McMurray, H.N. The Sacrificial Protection of Steel by Zinc-Containing Sol-Gel Coatings. *J. Electrochem. Soc.* **2019**, *166*, C434–C444. [CrossRef]
13. Figueira, R.B.; Silva, C.J.R.; Pereira, E.V. Organic–Inorganic Hybrid Sol–Gel Coatings for Metal Corrosion Protection: A Review of Recent Progress. *J. Coat. Technol. Res.* **2014**, *12*, 1–35. [CrossRef]
14. Touzin, M.; Béclin, F. Fabrication and Characterization of Composite Sol-Gel Coatings on Porous Ceramic Substrate. *J. Eur. Ceram. Soc.* **2011**, *31*, 1661–1667. [CrossRef]
15. Ma, Z.L.; Li, C.C.; Wei, H.M.; Ding, D.Q. Silica Sol-Gel Anchoring on Aluminum Pigments Surface for Corrosion Resistance Based on Aluminum Oxidized by Hydrogen Peroxide. *Dye. Pigment.* **2015**, *114*, 253–258. [CrossRef]
16. De Damborenea, J.; Pellegri, N.; de Sanctis, O.; Durán, A. Electrochemical Behaviour of SiO2 Sol-Gel Coatings on Stainless Steel. *J. Sol-Gel Sci. Technol.* **1995**, *4*, 239–244. [CrossRef]
17. Zheng, S.; Li, J. Inorganic-Organic Sol Gel Hybrid Coatings for Corrosion Protection of Metals. *J. Sol-Gel Sci. Technol.* **2010**, *54*, 174–187. [CrossRef]
18. Gonzalez, E.; Vejar, N.; Solis, R.; Muñoz, L.; Encinas, M.V.; Paez, M. Sol-Gel Films: Corrosion Protection Coating for Aluminium Alloy. In *Sol-Gel Method—Design and Synthesis of New Materials with Interesting Physical, Chemical and Biological Properties*; IntechOpen: London, UK, 2019.
19. Ashrafi-Shahri, S.M.; Ravari, F.; Seifzadeh, D. Smart Organic/Inorganic Sol-Gel Nanocomposite Containing Functionalized Mesoporous Silica for Corrosion Protection. *Prog. Org. Coat.* **2019**, *133*, 44–54. [CrossRef]
20. Tiringer, U.; Durán, A.; Castro, Y.; Milošev, I. Self-Healing Effect of Hybrid Sol-Gel Coatings Based on GPTMS, TEOS, SiO2 Nanoparticles and Ce(NO3)3 Applied on Aluminum Alloy 7075-T6. *J. Electrochem. Soc.* **2018**, *165*, C213–C225. [CrossRef]
21. Alibakhshi, E.; Akbarian, M.; Ramezanzadeh, M.; Ramezanzadeh, B.; Mahdavian, M. Evaluation of the Corrosion Protection Performance of Mild Steel Coated with Hybrid Sol-Gel Silane Coating in 3.5 Wt.% NaCl Solution. *Prog. Org. Coat.* **2018**, *123*, 190–200. [CrossRef]
22. Bierwagen, G.P.; Allahar, K.; Hinderliter, B.; Jung, H. Zn-Rich Coatings Revisited. In Proceedings of the Tri-Service Corrosion Conference, Nashville, TN, USA, 11–15 March 2007.

23. Feliu, S., Jr.; Morcillo, M.; Feliu, S. Deterioration of Cathodic Protection Action of Zinc-Rich Paint Coatings in Atmospheric Exposure. *Corrosion* **2001**, *57*, 591–597. [CrossRef]
24. Theiler, F. The Rust Preventing Mechanism of Zinc Dust Paints. *Corros. Sci.* **1974**, *14*, 405–414. [CrossRef]
25. Kalendová, A. Effects of Particle Sizes and Shapes of Zinc Metal on the Properties of Anticorrosive Coatings. *Prog. Org. Coat.* **2003**, *46*, 324–332. [CrossRef]
26. Thomas, S.; Birbilis, N.; Venkatraman, M.S.; Cole, I.S. Self-Repairing Oxides to Protect Zinc: Review, Discussion and Prospects. *Corros. Sci.* **2013**, *69*, 11–22. [CrossRef]
27. Gergely, A.; Pászti, Z.; Mihály, J.; Drotár, E.; Török, T. Galvanic Function of Zinc-Rich Coatings Facilitated by Percolating Structure of the Carbon Nanotubes. Part II: Protection Properties and Mechanism of the Hybrid Coatings. *Prog. Org. Coat.* **2014**, *77*, 412–424. [CrossRef]
28. Akbarinezhad, E.; Ebrahimi, M.; Sharif, F.; Ghanbarzadeh, A. Evaluating Protection Performance of Zinc Rich Epoxy Paints Modified with Polyaniline and Polyaniline-Clay Nanocomposite. *Prog. Org. Coat.* **2014**, *77*, 1299–1308. [CrossRef]
29. Shirehjini, F.T.; Danaee, I.; Eskandari, H.; Zarei, D. Effect of Nano Clay on Corrosion Protection of Zinc-Rich Epoxy Coatings on Steel 37. *J. Mater. Sci. Technol.* **2016**, *32*, 1152–1160. [CrossRef]
30. Meroufel, A.; Deslouis, C.; Touzain, S. Electrochemical and Anticorrosion Performances of Zinc-Rich and Polyaniline Powder Coatings. *Electrochim. Acta* **2008**, *53*, 2331–2338. [CrossRef]
31. Gergely, A.; Török, T. Optimally Balanced Active-Passive Corrosion Protection by Zinc-Rich Paint Coatings Featuring Proper Hybrid Formulation with Polypyrrole Modified Carbon Nanotubes. *Mater. Sci. Forum* **2013**, *752*, 275–283. [CrossRef]
32. Gergely, A.; Pászti, Z.; Mihály, J.; Drotár, E.; Török, T. Galvanic Function of Zinc-Rich Coatings Facilitated by Percolating Structure of the Carbon Nanotubes. Part I: Characterization of the Nano-Size Particles. *Prog. Org. Coat.* **2015**, *78*, 437–445. [CrossRef]
33. Arman, S.Y.; Ramezanzadeh, B.; Farghadani, S.; Mehdipour, M.; Rajabi, A. Application of the Electrochemical Noise to Investigate the Corrosion Resistance of an Epoxy Zinc-Rich Coating Loaded with Lamellar Aluminum and Micaceous Iron Oxide Particles. *Corros. Sci.* **2013**, *77*, 118–127. [CrossRef]
34. Jalili, M.; Rostami, M.; Ramezanzadeh, B. An Investigation of the Electrochemical Action of the Epoxy Zinc-Rich Coatings Containing Surface Modified Aluminum Nanoparticle. *Appl. Surf. Sci.* **2015**, *328*, 95–108. [CrossRef]
35. Hoang, N.; Khoa, T.A.; Nhung, L.T.; Phuong, P.M.; Binh, T.D.; Hang, T.T.X.; Van Chi, N.; Nguyen, T.-D. Flake ZnAl Alloy as an Effective Pigment in Silicate Coatings for the Corrosion Protection of Steel. *Coatings* **2022**, *12*, 1046. [CrossRef]
36. Streitberger, H.-J.; Dössel, K.-F.; Werner Thomer, K.; Gehmecker, H.; Wonnemann, H.; Rink, H.-P.; Svejda, P.; Wilke, G.; Merz, P.W.; Burchardt, B.; et al. *Automotive Paints and Coatings*, 2nd ed.; Streitberger, H.-J., Dössel, K., Eds.; Wiley: Hoboken, NJ, USA, 2008.
37. Bohm, S.; Holness, R.J.; McMurray, H.N.; Worsley, D.A. Charge Percolation and Sacrificial Protection in Zinc-Rich Organic Coatings. In Proceedings of the Eurocorr'2000, Quenn Mary and Westfield College, London, UK, 10–14 September 2000.
38. Figueira, R.B.; Fontinha, I.R.; Silva, C.J.R.; Pereira, E.V. Hybrid Sol-Gel Coatings: Smart and Green Materials for Corrosion Mitigation. *Coatings* **2016**, *6*, 12. [CrossRef]
39. Meroufel, A.; Touzain, S. EIS Characterisation of New Zinc-Rich Powder Coatings. *Prog. Org. Coat.* **2007**, *59*, 197–205. [CrossRef]
40. Marchebois, H.; Savall, C.; Bernard, J.; Touzain, S. Electrochemical Behavior of Zinc-Rich Powder Coatings in Artificial Sea Water. *Electrochim. Acta* **2004**, *49*, 2945–2954. [CrossRef]
41. Zhang, L.; Ma, A.; Jiang, J.; Song, D.; Chen, J.; Yang, D. Anti-Corrosion Performance of Waterborne Zn-Rich Coating with Modified Silicon-Based Vehicle and Lamellar Zn (Al) Pigments. *Prog. Nat. Sci. Mater. Int.* **2012**, *22*, 326–333. [CrossRef]
42. Phan, T.T.; Bentiss, F.; Jama, C. Effects of Sol–Gel Process Parameters on the Anticorrosive Performance of Phosphosilicate Hybrid Coatings for Carbon Steel: Structural and Electrochemical Studies. *New J. Chem.* **2018**, *42*, 13442–13452. [CrossRef]
43. Phan, T.T.; Bentiss, F.; Jama, C. Structural and Anticorrosion Performance Characterization of Phosphosilicate Sol–Gel Coatings Prepared from 3-(Trimethoxysilyl) Propyl Methacrylate and Bis [2-(Methacryloyloxy)Ethyl] Phosphate. *Prog. Org. Coat.* **2015**, *89*, 123–131. [CrossRef]
44. Esbayou, M.; Bentiss, F.; Casetta, M.; Nyassi, A.; Jama, C. Optimization of Cold Plasma Process Parameters for Organosilicon Films Deposition on Carbon Steel: Study of the Surface Pretreatment Effect on Corrosion Protection Performance in 3 Wt% NaCl Medium. *J. Alloys Compd.* **2018**, *758*, 148–161. [CrossRef]
45. Jones, D. *Principles and Prevention of Corrosion*; Pearson: London, UK, 1992.
46. Hammouda, N.; Chadli, H.; Guillemot, G.; Belmokre, K. The Corrosion Protection Behaviour of Zinc Rich Epoxy Paint in 3% NaCl Solution. *Adv. Chem. Eng. Sci.* **2011**, *1*, 51–60. [CrossRef]
47. Moraga, G.A.; Silva, G.G.; Matencio, T.; Paniago, R.M. Poly(2,5-Dimethoxy Aniline)/Fluoropolymer Blend Coatings to Corrosion Inhibition on Stainless Steel. *Synth. Met.* **2006**, *156*, 1036–1042. [CrossRef]
48. Ouerd, A.; Alemany-Dumont, C.; Normand, B.; Szunerits, S. Reactivity of CoCrMo Alloy in Physiological Medium: Electrochemical Characterization of the Metal/Protein Interface. *Electrochim. Acta* **2008**, *53*, 4461–4469. [CrossRef]
49. Akbarinezhad, E.; Ebrahimi, M.; Faridi, H.R. Corrosion Inhibition of Steel in Sodium Chloride Solution by Undoped Polyaniline Epoxy Blend Coating. *Prog. Org. Coat.* **2009**, *64*, 361–364. [CrossRef]
50. Creus, J.; Idrissi, H.; Mazille, H. Galvanic Corrosion Behaviour of Mild Steel, Al, and Ti in 3%NaCl Solution: Application to PVD Coatings on Steel Substrate. *Surf. Eng.* **1997**, *13*, 415–419. [CrossRef]
51. Yang, J.; Lu, Y.; Guo, Z.; Gu, J.; Gu, C. Corrosion Behaviour of a Quenched and Partitioned Medium Carbon Steel in 3.5 Wt.% NaCl Solution. *Corros. Sci.* **2018**, *130*, 64–75. [CrossRef]

52. Marchebois, H.; Joiret, S.; Savall, C.; Bernard, J.; Touzain, S. Characterization of Zinc-Rich Powder Coatings by EIS and Raman Spectroscopy. *Surf. Coat. Technol.* **2002**, *157*, 151–161. [CrossRef]

53. Bastos, A.C.; Zheludkevich, M.L.; Klüppel, I.; Grundmeier, G.; Ferreira, M.G.S. Modification of Zinc Powder to Improve the Corrosion Resistance of Weldable Primers. *Prog. Org. Coat.* **2010**, *69*, 184–192. [CrossRef]

54. Mahdavian, M.; Attar, M.M. Another Approach in Analysis of Paint Coatings with EIS Measurement: Phase Angle at High Frequencies. *Corros. Sci.* **2006**, *48*, 4152–4157. [CrossRef]

55. Vilche, J.R.; Bucharsky, E.C.; Giúdice, C.A. Application of EIS and SEM to Evaluate the Influence of Pigment Shape and Content in ZRP Formulations on the Corrosion Prevention of Naval Steel. *Corros. Sci.* **2002**, *44*, 1287–1309. [CrossRef]

56. Nguyen, T.Q.; Breitkopf, C. Determination of Diffusion Coefficients Using Impedance Spectroscopy Data. *J. Electrochem. Soc.* **2018**, *165*, E826–E831. [CrossRef]

57. Kittel, J.; Celati, N.; Keddam, M.; Takenouti, H. New Methods for the Study of Organic Coatings by EIS. *Prog. Org. Coat.* **2001**, *41*, 93–98. [CrossRef]

58. McIntyre, J.M.; Pham, H.Q. Electrochemical Impedance Spectroscopy; a Tool for Organic Coatings Optimizations. *Prog. Org. Coat.* **1996**, *27*, 201–207. [CrossRef]

59. Marques, A.G.; Simões, A.M. EIS and SVET Assessment of Corrosion Resistance of Thin Zn-55% Al-Rich Primers: Effect of Immersion and of Controlled Deformation. *Electrochim. Acta* **2014**, *148*, 153–163. [CrossRef]

60. Xing, C.; Wang, W.; Qu, S.; Tang, Y.; Zhao, X.; Zuo, Y. Degradation of Zinc-Rich Epoxy Coating in 3.5% NaCl Solution and Evolution of Its EIS Parameters. *J. Coat. Technol. Res.* **2021**, *18*, 843–860. [CrossRef]

61. Muster, T.H.; Cole, I.S. The Protective Nature of Passivation Films on Zinc: Surface Charge. *Corros. Sci.* **2004**, *46*, 2319–2335. [CrossRef]

62. Song, D.; Wan, H.; Tu, X.; Li, W. A Better Understanding of Failure Process of Waterborne Coating/Metal Interface Evaluated by Electrochemical Impedance Spectroscopy. *Prog. Org. Coat.* **2020**, *142*, 105558. [CrossRef]

63. Zeng, Y.; Kang, L.; Wu, Y.; Wan, S.; Liao, B.; Li, N.; Guo, X. Melamine Modified Carbon Dots as High Effective Corrosion Inhibitor for Q235 Carbon Steel in Neutral 3.5 Wt% NaCl Solution. *J. Mol. Liq.* **2022**, *349*, 118108. [CrossRef]

64. Amirudin, A.; Thierry, D. Application of Electrochemical Impedance Spectroscopy to Study the Atmospheric Corrosion of Painted Metals. *Mater. Sci. Forum* **1995**, *192–194*, 317–334. [CrossRef]

65. Hsu, C.H.; Mansfeld, F. Technical Note: Concerning the Conversion of the Constant Phase Element Parameter Y 0 into a Capacitance. *Corrosion* **2001**, *57*, 747–748. [CrossRef]

66. Bastos, A.C.; Simões, A.M.P. Effect of Deep Drawing on the Performance of Coil-Coatings Assessed by Electrochemical Techniques. *Prog. Org. Coat.* **2009**, *65*, 295–303. [CrossRef]

67. Feliu, S., Jr.; Bastidas, J.M.; Morcillo, M.; Feliu, S. Effect of the Di-Iron Phosphide Conductive Extender on the Protective Mechanisms of Zinc-Rich Coatings. *J. Coat. Technol.* **1991**, *63*, 67–72.

68. Cheng, L.; Liu, C.; Han, D.; Ma, S.; Guo, W.; Cai, H.; Wang, X. Effect of Graphene on Corrosion Resistance of Waterborne Inorganic Zinc-Rich Coatings. *J. Alloys Compd.* **2019**, *774*, 255–264. [CrossRef]

69. Volovitch, P.; Vu, T.N.; Allély, C.; Abdel Aal, A.; Ogle, K. Understanding Corrosion via Corrosion Product Characterization: II. Role of Alloying Elements in Improving the Corrosion Resistance of Zn-Al-Mg Coatings on Steel. *Corros. Sci.* **2011**, *53*, 2437–2445. [CrossRef]

70. Wallinder, I.O.; Leygraf, C.; Karlén, C.; Heijerick, D.; Janssen, C.R. Atmospheric Corrosion of Zinc-Based Materials: Runoff Rates, Chemical Speciation and Ecotoxicity Effects. *Corros. Sci.* **2001**, *43*, 809–816. [CrossRef]

71. Yoo, J.D.; Ogle, K.; Volovitch, P. The Effect of Synthetic Zinc Corrosion Products on Corrosion of Electrogalvanized Steel: I. Cathodic Reactivity under Zinc Corrosion Products. *Corros. Sci.* **2014**, *81*, 11–20. [CrossRef]

72. Salgueiro Azevedo, M.; Allély, C.; Ogle, K.; Volovitch, P. Corrosion Mechanisms of Zn(Mg,Al) Coated Steel: 2. The Effect of Mg and Al Alloying on the Formation and Properties of Corrosion Products in Different Electrolytes. *Corros. Sci.* **2015**, *90*, 482–490. [CrossRef]

73. Wan, B.; Yan, Y.; Huang, R.; Abdala, D.B.; Liu, F.; Tang, Y.; Tan, W.; Feng, X. Formation of Zn-Al Layered Double Hydroxides (LDH) during the Interaction of ZnO Nanoparticles (NPs) with γ-Al2O3. *Sci. Total Environ.* **2019**, *650*, 1980–1987. [CrossRef] [PubMed]

74. Li, L.; Pi, P.; Wen, X.; Cheng, J.; Yang, Z. Optimization of Sol–Gel Coatings on the Surface of Aluminum Pigments for Corrosion Protection. *Corros. Sci.* **2008**, *50*, 795–803. [CrossRef]

75. Gallardo, J.; Galliano, P.; Durán, A. Thermal Evolution of Hybrid Sol-Gel Silica Coatings: A Structural Analysis. *J. Sol.-Gel Sci. Technol.* **2000**, *19*, 393–397. [CrossRef]

76. Persson, D.; Thierry, D.; LeBozec, N.; Prosek, T. In Situ Infrared Reflection Spectroscopy Studies of the Initial Atmospheric Corrosion of Zn-Al-Mg Coated Steel. *Corros. Sci.* **2013**, *72*, 54–63. [CrossRef]

77. Zhu, F.; Zhang, X.; Persson, D.; Thierry, D. In Situ Infrared Reflection Absorption Spectroscopy Studies of Confined Zinc Surfaces Exposed under Periodic Wet-Dry Conditions. *Electrochem. Solid-State Lett.* **2001**, *4*, 19–22. [CrossRef]

78. Prosek, T.; Nazarov, A.; Bexell, U.; Thierry, D.; Serak, J. Corrosion Mechanism of Model Zinc-Magnesium Alloys in Atmospheric Conditions. *Corros. Sci.* **2008**, *50*, 2216–2231. [CrossRef]

79. Nguyen, T.; Byrd, E.; Bentz, D.; Lin, C. In Situ Measurement of Water at the Organic Coating/Substrate Interface. *Prog. Org. Coat.* **1996**, *27*, 181–193. [CrossRef]

80. Haldhar, R.; Parveen Asrafali, S.; Jayprakash Raorane, C.; Periyasamy, T.; Kim, S.C. Performance of Cross-Linked Polymers as a Potential Anticorrosive Coating for Low Carbon Steel in Acidic Condition: Experimental and Computational Studies. *J. Mol. Liq.* **2022**, *360*, 119384. [CrossRef]

81. Mahjoubi, F.Z.; Khalidi, A.; Abdennouri, M.; Barka, N. Zn–Al Layered Double Hydroxides Intercalated with Carbonate, Nitrate, Chloride and Sulphate Ions: Synthesis, Characterisation and Dye Removal Properties. *J. Taibah Univ. Sci.* **2017**, *11*, 90–100. [CrossRef]

82. Seftel, E.M.; Popovici, E.; Mertens, M.; De Witte, K.; Van Tendeloo, G.; Cool, P.; Vansant, E.F. Zn-Al Layered Double Hydroxides: Synthesis, Characterization and Photocatalytic Application. *Microporous Mesoporous Mater.* **2008**, *113*, 296–304. [CrossRef]